



Universiteit
Leiden
The Netherlands

The magnetic field and multiple planets of the young dwarf AU Mic
Donati, J.-F.; Cristofari, P.I.; Finocietty, B.; Klein, B.; Moutou, C.; Gaidos, E.; ... ; Folsom, C.P.

Citation

Donati, J. -F., Cristofari, P. I., Finocietty, B., Klein, B., Moutou, C., Gaidos, E., ... Folsom, C. P. (2023). The magnetic field and multiple planets of the young dwarf AU Mic. *Monthly Notices Of The Royal Astronomical Society*, 525(1), 455-475. doi:10.1093/mnras/stad1193












Version: Publisher's Version

License: [Creative Commons CC BY 4.0 license](https://creativecommons.org/licenses/by/4.0/)

Downloaded from: <https://hdl.handle.net/1887/3719270>

Note: To cite this publication please use the final published version (if applicable).

The magnetic field and multiple planets of the young dwarf AU Mic

J.-F. Donati ¹★, P. I. Cristofari ¹, B. Finocciety ¹, B. Klein ^{1,2}, C. Moutou,¹ E. Gaidos ³, C. Cadieux,⁴ E. Artigau,⁴ A. C. M. Correia ^{5,6}, G. Boué ⁶, N. J. Cook ⁴, A. Carmona,⁷ L. T. Lehmann ¹, J. Bouvier,⁷ E. Martioli,^{8,9} J. Morin ¹⁰, P. Fouqué,¹ X. Delfosse,⁷ R. Doyon,⁴ G. Hébrard,⁹ S. H. P. Alencar,¹¹ J. Laskar,⁶ L. Arnold,¹² P. Petit,¹ Á. Kóspál,¹³ A. Vidotto ¹⁴, C. P. Folsom¹⁵
and the SLS collaboration

¹Univ. de Toulouse, CNRS, IRAP, 14 avenue Belin, 31400 Toulouse, France

²Sub-department of Astrophysics, Department of Physics, University of Oxford, Oxford OX1 3RH, UK

³Department of Earth Sciences, University of Hawai'i at Manoa, 1680 East-West Road, Honolulu, HI 96822, USA

⁴Département de Physique, Université de Montréal, IREX, Montréal, QC H3C 3J7, Canada

⁵CFisUC, Departamento de Física, Universidade de Coimbra, 3004-516 Coimbra, Portugal

⁶IMCCE, CNRS, Obs. de Paris, Sorbonne Univ., 77 av. Denfert-Rochereau, 75014 Paris, France

⁷Univ. Grenoble Alpes, CNRS, IPAG, 38000 Grenoble, France

⁸Laboratório Nacional de Astrofísica, Rua Estados Unidos 154, 37504-364 Itajubá, MG, Brazil

⁹Institut d'Astrophysique de Paris, CNRS, Sorbonne Univ., 98 bis bd Arago, 75014 Paris, France

¹⁰LUPM, Univ. de Montpellier, CNRS, F-34095 Montpellier, France

¹¹Departamento de Física – ICEx – UFMG, Av. Antônio Carlos, 6627, 30270-901 Belo Horizonte, MG, Brazil

¹²Canada-France-Hawaii Telescope, 65-1238 Mamalahoa Hwy., Kamuela, HI 96743, USA

¹³Konkoly Observatory, Research Centre for Astronomy and Earth Sciences, Konkoly-Thege Miklós út 15-17, 1121 Budapest, Hungary

¹⁴Leiden Observatory, Leiden University, Niels Bohrweg 2, 2333 CA Leiden, the Netherlands

¹⁵Tartu Observatory, University of Tartu, Observatooriumi 1, 61602 Tõravere, Estonia

Accepted 2023 April 17. Received 2023 April 17; in original form 2023 February 10

ABSTRACT

In this paper, we present an analysis of near-infrared spectropolarimetric and velocimetric data of the young M dwarf AU Mic, collected with SPIRou at the Canada–France–Hawaii telescope from 2019 to 2022, mostly within the SPIRou Legacy Survey. With these data, we study the large- and small-scale magnetic field of AU Mic, detected through the unpolarized and circularly polarized Zeeman signatures of spectral lines. We find that both are modulated with the stellar rotation period (4.86 d), and evolve on a time-scale of months under differential rotation and intrinsic variability. The small-scale field, estimated from the broadening of spectral lines, reaches 2.61 ± 0.05 kG. The large-scale field, inferred with Zeeman–Doppler imaging from Least-Squares Deconvolved profiles of circularly polarized and unpolarized spectral lines, is mostly poloidal and axisymmetric, with an average intensity of 550 ± 30 G. We also find that surface differential rotation, as derived from the large-scale field, is ≈ 30 per cent weaker than that of the Sun. We detect the radial velocity (RV) signatures of transiting planets b and c, although dwarfed by activity, and put an upper limit on that of candidate planet d, putatively causing the transit-timing variations of b and c. We also report the detection of the RV signature of a new candidate planet (e) orbiting further out with a period of 33.39 ± 0.10 d, i.e. near the 4:1 resonance with b. The RV signature of e is detected at 6.5σ while those of b and c show up at $\approx 4\sigma$, yielding masses of $10.2^{+3.9}_{-2.7}$ and $14.2^{+4.8}_{-3.5} M_{\oplus}$ for b and c, and a minimum mass of $35.2^{+6.7}_{-5.4} M_{\oplus}$ for e.

Key words: techniques: polarimetric – stars: formation – stars: imaging – stars: individual: AU Mic – stars: magnetic field – planetary systems.

1 INTRODUCTION

The formation of stars and their planets has become a very popular forefront topic of modern astrophysics, following the discovery of thousands of exoplanetary systems and the availability of many new powerful instruments capable of characterizing them, such as the JWST most recently. The goal of such studies is to investigate the

surprising diversity of the exoplanetary systems detected around low-mass stars, and in particular to better understand the formation and evolution of planetary systems like ours. Studying newly born planetary systems and their pre-main-sequence (PMS) host stars is essential in this respect, the first evolutionary steps being those for which, we currently have no more than weak observational constraints to guide theoretical models.

So far, very few multiple planetary systems younger than 50 Myr have been reported around low-mass stars, two of which detected with transit photometry, namely V1298 Tau (hosting 4 transiting

* E-mail: jean-francois.donati@irap.omp.eu

planets; David et al. 2019) and AU Mic (with 2 known transiting warm Neptunes; Plavchan et al. 2020; Martioli et al. 2021; Szabó et al. 2021, 2022), then further monitored with precision Doppler velocimetry (Klein et al. 2021; Suárez Mascareño et al. 2021; Zicher et al. 2022). Given that young low-mass stars are usually quite active and strongly magnetic as a result of their short rotation periods (and convective envelopes), investigating their planets mandatorily requires characterization of the magnetic activity of the star so that the impact of this activity can be taken into account, and filtered out from the radial velocity (RV) curves in which planetary signatures hide. Constraining the large-scale magnetic fields of PMS stars is also essential for further documenting the parent dynamo processes that are able to amplify and sustain these fields, for investigating star-disc interactions and angular momentum evolution for stars whose accretion disc is still present (e.g. Zanni & Ferreira 2013; Blinova, Romanova & Lovelace 2016), and for studying potential star-planet interactions that may occur if the planets orbit within the Alfvén radius of their host stars (e.g. Strugarek et al. 2015). In this paper, we focus on the second and the brightest of these 2 stars, i.e. AU Mic.

AU Mic is an active M1 dwarf that belongs to the β Pic moving group (aged $\simeq 20$ Myr; Mamajek & Bell 2014; Miret-Roig et al. 2020). Hosting an extended debris disc with moving features (Kalas, Liu & Matthews 2004; Boccaletti et al. 2015, 2018) and 2 known transiting warm Neptunes (Plavchan et al. 2020; Martioli et al. 2021), it is an ideal target for studying the formation and evolution of young planets and their atmospheres (Hirano et al. 2020). Several studies focused on estimating the masses of both planets, the 2 latest ones yielding $M_b = 14.3 \pm 7.7 M_\oplus$ (where M_\oplus notes the Earth mass) and $M_c = 34.9 \pm 10.8$ (Klein et al. 2022), and $M_b = 11.7 \pm 5.0 M_\oplus$ and $M_c = 22.2 \pm 6.7$ (Zicher et al. 2022). Given the large transit-timing variations (TTVs) of up to ± 10 min reported for planets b and c (Szabó et al. 2022), it is likely that the planetary system of AU Mic includes more, yet undetected, bodies. A new candidate Earth-mass planet (dubbed d), putatively located between b and c, was recently proposed to account for the reported TTVs (Wittrock et al. 2023). Besides, AU Mic is known for its intense activity and strong magnetic field (Kochukhov & Reiners 2020; Klein et al. 2021), making it a prime target for studying dynamos of largely convective stars, magnetized winds, and star-planet interactions (Kavanagh et al. 2021; Alvarado-Gómez et al. 2022; Klein et al. 2022), or escaping planetary atmospheres (Carolan et al. 2020).

In this paper, we report extended near-infrared (nIR) high-resolution spectropolarimetric observations of AU Mic with SPIRou at the 3.6-m Canada–France–Hawaii Telescope (CFHT) atop Maunakea in Hawaii, from early 2019 to mid 2022. After outlining our observations and data reduction in Section 2, we briefly revisit the main parameters of AU Mic in Section 3, compute the longitudinal and small-scale magnetic fields and their modulation with time in Section 4, carry out Zeeman–Doppler Imaging (ZDI) of our spectropolarimetric data at the main observing epochs in Section 5, study and model RV variations in Section 6, and investigate several activity proxies in Section 7. We finally summarize and discuss our results, and conclude by suggesting follow-up studies in Section 8.

2 SPIROU OBSERVATIONS

AU Mic was intensively observed from early 2019 to mid 2022 with the SPIRou nIR spectropolarimeter/high-precision velocimeter (Donati et al. 2020) at CFHT, mostly within the SPIRou Legacy Survey (SLS), a Large Programme of 310 nights with SPIRou focussing on planetary systems around nearby M dwarfs on the

one hand, and on the study of magnetized star/planet formation on the other. SPIRou collects spectra covering the entire 0.95–2.50 μm wavelength range in a single exposure, at a resolving power of 70 000, and for any given polarization state. A total of 235 circular polarization sequences on 194 different nights were collected on AU Mic with SPIRou over this 3-yr period, 181 in the framework of the SLS itself, 38 within the Director’s Discretionary Time PI program of Baptiste Klein (run ID 19AD97 and 19BD97, with results published in Klein et al. 2021), 15 within the PI program of Eric Gaidos (run ID 20AH93) and 1 within the PI program of Julien Morin (run ID 19AF26). As outlined in Donati et al. (2020), each SPIRou polarization sequence consists of 4 sub-exposures (except for one featuring 2 sub-exposures only due to bad weather). Each sub-exposure is associated with a different orientation of the Fresnel rhomb retarders (to remove systematics in polarization spectra to first order, see Donati et al. 1997), yielding one unpolarized (Stokes I) and one circularly polarized (Stokes V) spectrum. A series of 29 such spectra were also collected during the transit of AU Mic b on 2019 June 16, thanks to which Martioli et al. (2020) demonstrated, via the Rossiter–McLaughlin effect, that the planet orbit is prograde and lies in the equatorial plane of the host star (within 15°) and in the plane of the debris disc (Boccaletti et al. 2018).

With 10 of the 235 spectra collected in bad weather conditions and featuring much lower signal-to-noise ratio (SNR), we are left with a total of 225 Stokes I and V spectra of AU Mic collected on 188 different nights. Exposure times for most sequences are $\simeq 800$ s, except for a few of them (e.g. those collected during the transit of AU Mic b) that were shorter (from 380 to 490 s). Peak SNRs range from 407 to 954 (median 785). The full log of our SPIRou observations is provided in Table A1 as supplementary material.

All data were processed with a new version of LIBRE ESPRIT, the nominal reduction pipeline of ESPaDOnS at CFHT, adapted for SPIRou (Donati et al. 2020). These reduced spectra were used in particular for the spectropolarimetric analyses outlined in Sections 4 and 5. Least-Squares Deconvolution (LSD; Donati et al. 1997) was then applied to all reduced spectra, using a line mask constructed from the VALD-3 data base (Ryabchikova et al. 2015) for an effective temperature $T_{\text{eff}} = 3750$ K and a logarithmic surface gravity $\log g = 4.5$ adapted to young early M dwarfs like AU Mic (see Section 3), and selecting lines of relative depths larger than 3 per cent only (for a total of $\simeq 1500$ lines, featuring an average Landé factor of 1.2). The noise levels σ_V in the resulting Stokes V LSD profiles range from 0.73 to 1.73 (median 0.96) in units of $10^{-4} I_c$ where I_c notes the continuum intensity. We also applied LSD to our spectra using 2 sub-masks of our main line mask, the high-Landé mask including lines with Landé factors larger than 1.5 (average Landé factor 1.7), and the low-Landé mask including lines with Landé factors lower than 1.0 (average Landé factor 0.7), both sub-masks featuring more or less the same number of lines ($\simeq 300$) and the same average wavelength as the main mask ($\simeq 1700$ nm).

In parallel, our data were also processed with APERO (version 0.7.275), the nominal SPIRou reduction pipeline (Cook et al. 2022), currently better optimized in terms of RV precision than LIBRE ESPRIT. The reduced spectra were then analysed by the line-by-line (LBL) technique (version 0.45, Artigau et al. 2022) to compute precise RVs for 185 of the 188 nightly averaged observations collected on AU Mic,¹ with a median RV error bar of 3.8 m s^{-1} (see Table A1). Our RV data were also corrected for an overall trend,

¹Three spectra suffered from an instrumental issue that affected the SPIRou RV reference module, yielding no precise RV estimates at these dates.

called Zero Point and coming from both the instrument and the reduction. It is inferred from a Gaussian Process Regression (GPR) applied to the RV curves of a dozen RV standard stars regularly monitored with SPIRou, and whose amplitude is small (RMS of a few m s^{-1}) with respect to the measured RV variations of AU Mic. Finally, in addition to RVs, the LBL analysis produces other diagnostics, in particular, one measuring the variations in the average width of line profiles with respect to the median spectrum, which serves as an activity proxy (called differential line width or dLW in Artigau et al. 2022) linked to the Zeeman broadening of unpolarized spectra (see Section 4). These data were used for the RV analysis detailed in Section 6, and in the following section on activity proxies (Section 7).

3 FUNDAMENTAL PARAMETERS OF AU MIC

AU Mic (Gl 803, HD 197481, HIP 102409, $V = 8.627$, $J = 5.436$) is a bright M1p.m.S dwarf located at a distance of 9.714 ± 0.002 pc from us (Gaia Collaboration 2021), with a rotation period of 4.86 d (Plavchan et al. 2020; Klein et al. 2021; Zicher et al. 2022), typical of its young age (≈ 20 Myr, Mamajek & Bell 2014; Miret-Roig et al. 2020). As usual for young active M dwarfs, it exhibits photometric fluctuations caused by surface brightness inhomogeneities and flares, with an amplitude of a few per cent (e.g. Plavchan et al. 2020; Martioli et al. 2021). Its mean $V-I$ colour (equal to 2.034 ± 0.060 mag, Kiraga 2012) yields $T_{\text{eff}} = 3700 \pm 70$ K (Pecaut & Mamajek 2013), consistent with previous estimates (Gaidos et al. 2014; Malo et al. 2014; Afram & Berdyugina 2019; Maldonado et al. 2020, quoting 3742 ± 83 , 3642 ± 22 , $3700 - 3800$, and 3755 ± 69 K, respectively). It implies that AU Mic has a bolometric magnitude of 7.22 ± 0.02 mag and therefore a logarithmic luminosity with respect to the Sun $\log L_*/L_\odot = -0.99 \pm 0.01$, in agreement with, e.g. Malo et al. (2014) and Cifuentes et al. (2020). The inferred radius is $R_* = 0.78 \pm 0.04 R_\odot$.

The most recent interferometric measurements suggest a radius of $0.862 \pm 0.052 R_\odot$ (when taking into account limb darkening, Gallenne et al. 2022), slightly larger though still compatible with the previous value within 1σ . Given the rotation period of 4.86 ± 0.01 d (the error bar indicating temporal variability rather than precision), these two R_* estimates translate into line-of-sight-projected rotation velocities at the equator of $v \sin i = 8.1 \pm 0.2$ and $9.0 \pm 0.5 \text{ km s}^{-1}$, respectively (AU Mic being seen almost equator on, Martioli et al. 2020, 2021). From a fit to infrared spectral lines (including magnetic broadening), Kochukhov & Reiners (2020) find $v \sin i = 9.2 \pm 0.1 \text{ km s}^{-1}$, consistent with the interferometric radius, although the authors mention that a smaller $v \sin i$ (of 8.1 km s^{-1}) is also possible when assuming a larger macroturbulence velocity (both being hard to determine independently). This further argues in favour of a radius in the range $0.80\text{--}0.85 R_\odot$ for AU Mic.

We used our spectra to redetermine the parameters of AU Mic with the tool designed for characterizing SPIRou spectra of M dwarfs (Cristofari et al. 2022a,b). Since magnetic fields significantly contribute to the width of spectral lines in stars as active and magnetic as AU Mic (López-Valdivia et al. 2021), we implemented polarized radiative transfer in the modelling (see Cristofari et al. 2023, and references therein for more information on the method) and carried out the analysis on the median SPIRou spectrum of AU Mic, including the effect of small-scale magnetic fields as in Kochukhov & Reiners (2020). In practice, we computed a grid of model spectra for different atmospheric parameters (T_{eff} , $\log g$, metallicity [M/H], abundance of α elements relative to Fe [α/Fe]) and magnetic strengths (0, 2, 4, 6, 8, and 10 kG, assuming in each

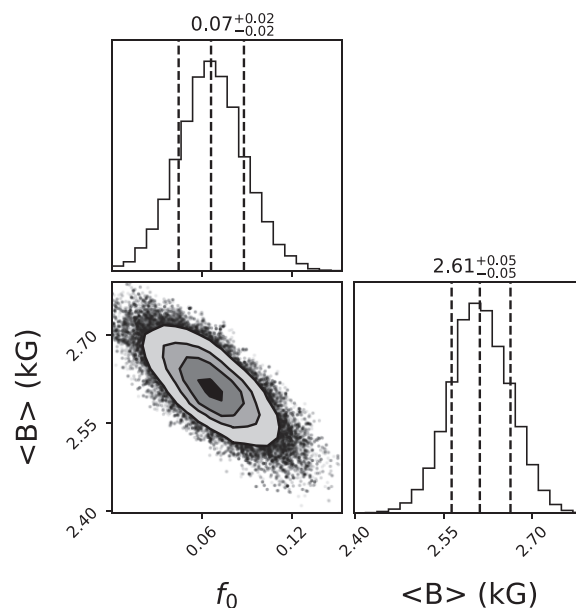


Figure 1. Magnetic parameters of AU Mic, derived by fitting our median SPIRou spectrum using the atmospheric modeling approach of Cristofari et al. (2023), which incorporates magnetic fields as well as an MCMC process to determine optimal parameters and their error bars. We find that AU Mic hosts a small-scale magnetic field of $\langle B \rangle = 2.61 \pm 0.05$ kG, whereas the relative area of non-magnetic regions at the surface of the star is $f_0 = 0.07 \pm 0.02$.

case a radial field of equal strength over the star), and ran a Monte Carlo Markov Chain (MCMC) process to find the atmospheric parameters and combination of magnetic spectra that best match the profiles of selected atomic and molecular lines with various magnetic sensitivities (including the Ti lines used by Kochukhov & Reiners 2020 and the field insensitive CO lines at $2.3 \mu\text{m}$).

For the main atmospheric parameters, we find that $T_{\text{eff}} = 3665 \pm 31$ K, $\log g = 4.52 \pm 0.05$, $[\text{M}/\text{H}] = 0.12 \pm 0.10$ and $[\alpha/\text{Fe}] = 0.00 \pm 0.04$. For the magnetic properties, we infer that the mean small-scale field at the surface of the star is $\langle B \rangle = 2.61 \pm 0.05$ kG whereas the optimal coefficient associated with the non-magnetic spectrum f_0 , i.e. the relative stellar surface area featuring no magnetic fields, is $f_0 = 0.07 \pm 0.02$ (see Fig. 1). Most of the reconstructed field concentrates within the 2 and 4 kG bins (with respective filling factors $f_2 = 59\%$ and $f_4 = 33\%$), whereas the 6, 8, and 10 kG bins ($f_6 = 1\%$, $f_8 = f_{10} = 0$) can be ignored (Cristofari et al. 2023). We stress that taking magnetic fields into account is important to derive reliable atmospheric parameters of stars as magnetic as AU Mic, with potential overestimates, especially in $\log g$, when the effect of magnetic fields is neglected (Cristofari et al. 2023). The magnetic field at the times of our observations is stronger and covers a larger fraction of the star than at the time of the observations of Kochukhov & Reiners (2020).

Comparing the temperature and luminosity derived above (implying together a radius of $0.79 \pm 0.02 R_\odot$) with the evolutionary models of Siess, Dufour & Forestini (2000, assuming solar metallicity and including overshoot) yields a mass of $M_* = 0.43 \pm 0.03 M_\odot$, a radius of $R_* = 0.74 \pm 0.03 R_\odot$ and an age of 13 ± 2 Myr, which is lower than the age of the β Pic moving group. Comparing now to the Baraffe et al. (2015) models gives a better agreement, with $M_* = 0.55 \pm 0.05 M_\odot$, $R_* = 0.78 \pm 0.02 R_\odot$ and an age of 17 ± 4 Myr. Using the Dartmouth models (assuming again solar metallicity and including overshoot, Dotter et al. 2008) further improves the match

Table 1. Parameters of AU Mic used in/derived from our study.

distance (pc)	9.714 ± 0.002	Gaia Collaboration (2021)
V (mag)	8.627 ± 0.052	Kiraga (2012)
$V - I$ (mag)	2.034 ± 0.060	Kiraga (2012)
J (mag)	5.436 ± 0.017	Cutri et al. (2003)
BC_J (mag)	1.72 ± 0.01	Pecaut & Mamajek (2013)
$\log(L_*/L_\odot)$	-0.99 ± 0.01	from T_{eff} , J , BC_J and distance
T_{eff} (K)	3665 ± 31	
$\log g$ (dex)	4.52 ± 0.05	4.39 ± 0.05 from mass and radius
$[M/H]$ (dex)	0.12 ± 0.10	
$[\alpha/\text{Fe}]$ (dex)	0.00 ± 0.04	
M_* (M_\odot)	0.60 ± 0.04	using Dotter et al. (2008)
R_* (R_\odot)	0.82 ± 0.02	
age (Myr)	23 ± 3	Mamajek & Bell (2014)
	18.5 ± 2.4	Miret-Roig et al. (2020)
P_{rot} (d)	4.86	period used to phase data
P_{rot} (d)	4.856 ± 0.003	period from B_ℓ data
P_{rot} (d)	4.866 ± 0.004	period from RV data
$v \sin i$ (km s^{-1})	8.5 ± 0.2	from P_{rot} and R_*
i	80°	assumed for ZDI
$\langle B \rangle$ (kG)	2.61 ± 0.05	orbit of b, Martioli et al. (2021)
f_0	0.07 ± 0.02	$f_2 = 59\%$, $f_4 = 33\%$
Ω_{eq} (rad d^{-1})	1.299 ± 0.002	average over 2020 and 2021
$d\Omega$ (mrad d^{-1})	37 ± 7	idem

with the measured parameters, yielding $M_* = 0.59 \pm 0.04 M_\odot$, $R_* = 0.79 \pm 0.02 R_\odot$, and an age of 20 ± 5 Myr. All predicted radii are smaller than, though still reasonably close to, the interferometric one. In fact, active M dwarfs have repeatedly been reported to exhibit inflated radii with respect to theoretical models, possibly under the effect of magnetic fields (Chabrier, Gallardo & Baraffe 2007; Morales et al. 2010; Feiden 2016), although there is no consensus on this point yet (e.g. Morrell & Naylor 2019).

We assume $M_* = 0.60 \pm 0.04 M_\odot$ and $R_* = 0.82 \pm 0.02 R_\odot$ for AU Mic in the rest of the paper, implying $v \sin i = 8.5 \pm 0.2$. The corresponding $\log g$ (4.39 ± 0.05) is slightly smaller than the one we measured, further arguing in favour of the Dartmouth models which yield a larger mass and thus a larger $\log g$ (4.42 ± 0.05) than the two others. Part of the discrepancy may also come from the fact that the standard atmospheric models we used to fit our SPIRou spectra may not be well adapted for young stars as strongly active and magnetic as AU Mic. We finally note that AU Mic is predicted to be still fully convective by the models of Siess et al. (2000), but to have already developed a small radiative core (of approximate mass and radius $0.2 M_*$ and $0.3 R_*$) in the models of Baraffe et al. (2015) and Dotter et al. (2008).

Parameters used in the following sections are listed in Table 1. Rotation cycles are computed using a rotation period of 4.86 d, and an arbitrary reference barycentric Julian date of $\text{BJD}_0 = 2459000$. (Note that a different BJD_0 was used in Klein et al. 2021, causing phases in our study to be 0.394 rotation cycle larger for profiles common to both studies.)

4 THE LONGITUDINAL FIELD AND ZEEMAN BROADENING OF AU MIC

Using the Stokes V and I LSD profiles of AU Mic computed in Section 2, we computed the longitudinal field B_ℓ , i.e. the line-of-sight-projected component of the vector magnetic field averaged over the visible hemisphere, following Donati et al. (1997). The Stokes V LSD signatures of AU Mic being quite broad, the first

moment is computed over a domain of $\pm 45 \text{ km s}^{-1}$ about the line centre, whereas the equivalent width of the Stokes I LSD profiles is simply estimated through a Gaussian fit (and found to be $\simeq 2 \text{ km s}^{-1}$). We also computed a null polarization check called N (Donati et al. 1997), and derived a mean longitudinal field from this check, which is expected to be equal to 0 within the error bars and to yield a reduced chi-square χ_r^2 close to 1.

We thus obtained 225 B_ℓ points over the full 3-yr timespan of our observations (see Table A1 for a complete log), as well as an equal number of values from the N profiles. The corresponding χ_r^2 from B_ℓ values and its equivalent from the N profiles are respectively equal to 500 and 0.95 over the whole series, confirming that the field is detected and that the error bars are consistent with photon noise. We find that B_ℓ ranges from -240 to 260 G, i.e. about an order of magnitude smaller than the average small-scale field $\langle B \rangle$ (see Section 3). We then carried out a quasi-periodic (QP) GPR fit to the B_ℓ curve, with the covariance function $c(t, t')$ set to

$$c(t, t') = \theta_1^2 \exp \left(-\frac{(t - t')^2}{2\theta_3^2} - \frac{\sin^2 \left(\frac{\pi(t - t')}{\theta_2} \right)}{2\theta_4^2} \right) \quad (1)$$

where θ_1 is the amplitude (in G) of the Gaussian Process (GP), θ_2 its recurrence period (very close to P_{rot}), θ_3 the evolution time-scale on which the B_ℓ curve changes shape (in d), and θ_4 a smoothing parameter setting the amount of allowed harmonic complexity. To these 4 hyper parameters, we added a fifth one called θ_5 that describes the additional uncorrelated noise that is needed to obtain the QP GPR fit to the B_ℓ data (denoted y) featuring the highest likelihood \mathcal{L} , defined by:

$$2 \log \mathcal{L} = -n \log(2\pi) - \log |C + \Sigma + S| - y^T (C + \Sigma + S)^{-1} y \quad (2)$$

where C is the covariance matrix for all observing epochs, Σ the diagonal variance matrix associated with y , $S = \theta_5^2 I$ the contribution of the additional white noise with I the identity matrix, and n the number of data points. Coupling this with an MCMC run to explore the parameter domain, we can determine the optimal set of hyper parameters and their posterior distributions/error bars.

The result of the fit is shown in Fig. 2 (top panel), with a zoom on seasons 2020 and 2021 also provided in the medium and bottom panels. The fitted GP parameters and error bars are listed in the top section of Table 2. All parameters are well defined, in particular the recurrence period θ_2 , found to be equal to 4.856 ± 0.003 d (i.e. close to the estimates of Plavchan et al. 2020; Cale et al. 2021; Klein et al. 2021; Zicher et al. 2022) and the evolution time-scale, which we measure at 80 ± 12 d, i.e. half the duration of a typical observing season. The data are fitted to a RMS level of 6.2 G, slightly larger than the average error bar on our B_ℓ measurements (of 5.2 G), yielding $\chi_r^2 = 1.4$. The B_ℓ data are thus not fitted down to the photon-noise level, suggesting an additional source of noise, e.g. intrinsic variability caused by activity (e.g. stochastic changes in the large-scale field, flares), modelled by the GP models with θ_5 being significantly different from 0. The season-to-season variations of B_ℓ are quite obvious, with the modulation shrinking to a minimum in October 2019 (BJD 2458800) and reaching a maximum in the following season (BJD 2459100). Moreover, as expected from the rather short evolution timescale, the fitted B_ℓ curve also evolves significantly within each season, as can be seen on, e.g. the middle panel of Fig. 2. Running GPR on the 2020 and 2021 data subsets further suggests that evolution was faster in 2020 ($\theta_3 = 73 \pm 11$ d) than in 2021 ($\theta_3 = 140 \pm 40$ d).

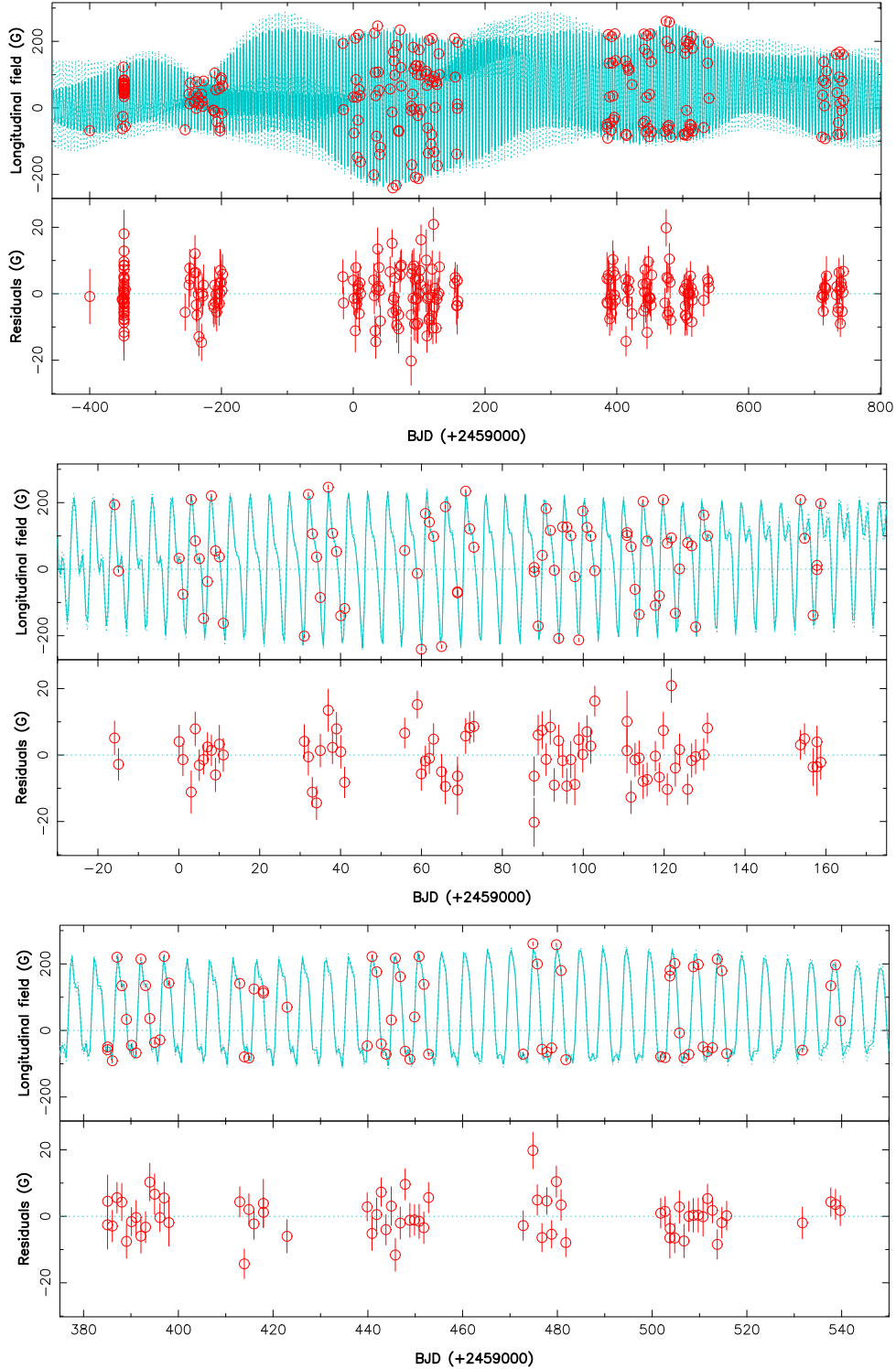


Figure 2. Longitudinal magnetic field B_ℓ of AU Mic (red dots) over our observing period, and QP GPR fit to the data (cyan). The residuals are shown in the bottom plot of each panel. The top panel show the whole data set, whereas the lower 2 panels present a zoom on the 2020 and 2021 data respectively. The RMS of the residuals is 6.2 G, slightly larger than the average error bar of 5.2 G, yielding $\chi_r^2 = 1.4$, whereas the χ_r^2 with respect to the weighted average is 442.

In parallel to the B_ℓ analysis, we used the new tool of Cristofari et al. (2023), with which we analysed the nightly medians of our Stokes I spectra (see Section 3), to derive the small-scale field at the stellar surface at each observing epoch and investigate its rotational modulation (freezing all non-magnetic parameters to the

values derived from the median spectrum, even though magnetic and non magnetic parameters are mostly uncorrelated). The derived values of $\langle B \rangle$ are listed in Table A1. As for B_ℓ , we carried out a QP GPR on the $\langle B \rangle$ values, resulting in a χ_r^2 of 0.17, i.e. much lower than 1. It reflects that the retrieved formal error bars are absolute

Table 2. Results of our MCMC modeling of the B_ℓ (first 5 rows) and $\langle B \rangle$ (last 5 rows) curves of AU Mic. For each hyper parameter, we list the fitted value along with the corresponding error bar, as well as the assumed prior. The knee of the modified Jeffreys prior is set to σ_B , i.e. the median error bars of our B_ℓ and $\langle B \rangle$ estimates (i.e. 5.2 and 20 G, respectively). For the recurrence period θ_2 , using a uniform prior yields the same result. For the evolution timescale θ_3 , the log Gaussian prior is set to 100 d (within a factor of 2), a typical value for early M dwarfs.

Parameter	Name	value	Prior
GP amplitude (G)	θ_1	100 ± 12	mod Jeffreys (σ_B)
Rec. period (d)	θ_2	4.856 ± 0.003	Gaussian (4.86, 0.1)
Evol. timescale (d)	θ_3	80 ± 12	log Gaussian (log 100, log 2)
Smoothing	θ_4	0.43 ± 0.04	Uniform (0, 3)
White noise (G)	θ_5	6.6 ± 0.9	mod Jeffreys (σ_B)
GP amplitude (kG)	θ_1	0.16 ± 0.03	mod Jeffreys (σ_B)
Rec. period (d)	θ_2	4.859 ± 0.004	Gaussian (4.86, 0.1)
Evol. timescale (d)	θ_3	153 ± 18	log Gaussian (log 100, log 2)
Smoothing	θ_4	0.71 ± 0.10	Uniform (0, 3)
White noise (kG)	θ_5	0.01 ± 0.01	mod Jeffreys (σ_B)

error bars (including systematics) rather than relative ones, thereby underestimating the precision at which night-to-night variations are measured. To derive relative error bars, we simply rescaled the formal ones using the dispersion of the residuals, thereby ensuring that the χ_r^2 of the QP GPR is close to 1 while θ_5 remains consistent with 0. We obtained the results shown in Fig. 3 and the hyper-parameters listed in the bottom section of Table 2, yielding now $\chi_r^2 = 0.78$.

We find that $\langle B \rangle$ is clearly modulated by the rotation cycle, with a recurrence period of 4.859 ± 0.004 d, i.e. marginally larger than the one derived from B_ℓ . The semi-amplitude of the modulation is small, less than 0.1 kG in 2020 and reaching a maximum of 0.25 kG in 2022. We note that the modulation of $\langle B \rangle$ is smallest when that of B_ℓ is largest and vice versa on our 4 observing seasons. Finally, the evolution time-scale is twice longer for $\langle B \rangle$ than for B_ℓ . Over our 4 seasons of observations, $\langle B \rangle$ decreases from about 2.80 kG down to about 2.65 kG (see Fig. 3) and is on average slightly larger than that estimated from the median spectrum (see Section 3). More specifically, this weakening shows up as a decrease of the fitted 4 kG coefficient f_4 , and a corresponding increase of the 2 kG coefficient f_2 (both being strongly anticorrelated, with a correlation coefficient $R = -0.90$). Whereas f_4 correlates with $\langle B \rangle$ ($R = 0.70$) and varies from 0.32 to 0.18, f_2 is anticorrelated with $\langle B \rangle$ ($R = -0.80$) and varies from 0.60 to 0.75. We also note that, as for B_ℓ , the evolution of $\langle B \rangle$ as derived by GPR is faster in 2020 ($\theta_3 = 90 \pm 30$ d) than in 2021 ($\theta_3 = 300 \pm 100$ d). These results illustrate that both B_ℓ and $\langle B \rangle$, probing different characteristics of the field, are quite useful and very complementary to analyse the magnetic properties of active stars like AU Mic.

We also looked at the Stokes I LSD profiles computed with the high-Landé and the low-Landé masks. We find that the profiles from the first set are clearly broader than those from the second set as a result of Zeeman broadening, with the median full-width-at-half-maximum (FWHM) of the high-Landé and low-Landé LSD profiles being respectively equal to 31.9 and 22.5 km s⁻¹. The amount of quadratic differential broadening between the 2 sets of profiles is found to be 22.6 ± 1.0 km s⁻¹ on average, with no clear evolution with time nor modulation with rotation phase. The FWHM of the high-Landé LSD profiles, dominated by Zeeman broadening, is weakly modulated by the rotation period and exhibits long-term variations of up to 2 km s⁻¹ over the full observing period. A GPR fit to the data yields a period of 4.85 ± 0.02 d and a semi-amplitude

of up to 1 km s⁻¹. A similar behaviour of about half the amplitude is observed on the FWHM of low-Landé LSD profiles. The overall trends on the FWHM of the LSD profile from high-Landé lines mimic those on $\langle B \rangle$, i.e. a small decrease over the 4 seasons and a minimum modulation amplitude in 2020. The correlation factor between FWHMs and $\langle B \rangle$ is found to be $R = 0.60$, suggesting that FWHMs can be used as an alternate proxy for $\langle B \rangle$, albeit with a loss of precision.

5 MAGNETIC FIELD AND DIFFERENTIAL ROTATION OF AU MIC

Using time-series of Stokes V and I LSD profiles, one can model the large-scale magnetic field at the surface of AU Mic, along with constraints on the small-scale field. This is achieved with ZDI, a tomographic imaging tool that inverts phase-resolved sets of LSD profiles into maps of the large-scale vector field (e.g. Donati et al. 2006; Klein et al. 2021). In the particular case of AU Mic, Stokes I LSD profiles are significantly broadened by magnetic fields and can be used to further constrain the magnetic map and give insights on the small-scale field.

5.1 Zeeman-Doppler Imaging

In practice, ZDI proceeds iteratively, starting from a null magnetic field and adding information as it explores the parameter space using conjugate gradient techniques. At each iteration, ZDI compares the synthetic Stokes profiles of the current magnetic image with observed ones, and loops until it reaches the requested level of agreement with the data (i.e. a given χ_r^2). As the problem is ill-posed and features an infinite number of solutions of variable complexity, we choose the simplest one, i.e. the solution with minimum information or maximum entropy that matches the data at the requested level (e.g. Skilling & Bryan 1984). The surface of the star is decomposed into 3000 grid cells. Local Stokes I and V profiles in each grid cell are computed using Unno–Rachkovsky’s equation of the polarized radiative transfer equation in a plane-parallel Milne Eddington atmosphere (Landí degl’Innocenti & Landolfi 2004), then integrated over the visible surface of the star at each observed rotation phase (assuming a linear center-to-limb darkening law for the continuum, with a coefficient of 0.3) to yield the synthetic profiles corresponding to the reconstructed image. The mean wavelength and Landé factor of our LSD profiles are 1700 nm and 1.2.

The magnetic field at the surface of the star is described through a spherical harmonics (SH) expansion, using the formalism of Donati et al. (2006) in which the poloidal and toroidal components of the vector field are expressed with 3 sets of complex SH coefficients, $\alpha_{\ell,m}$ and $\beta_{\ell,m}$ for the poloidal component, and $\gamma_{\ell,m}$ for the toroidal component², where ℓ and m note the degree and order of the corresponding SH term in the expansion.

ZDI can also model brightness inhomogeneities at the surface of the star, simultaneously with large-scale magnetic fields. In the particular case of AU Mic, we find that the distortions, and especially the broadening, of the LSD Stokes I profiles are dominated by magnetic effects, with only a small impact of surface brightness

²After a few years, the expressions of Donati et al. (2006) were modified to achieve a more consistent description of the field, with $\beta_{\ell,m}$ being replaced by $\alpha_{\ell,m} + \beta_{\ell,m}$ in the equations of the meridional and azimuthal field components (see, e.g. Finocciety & Donati 2022; Lehmann & Donati 2022).

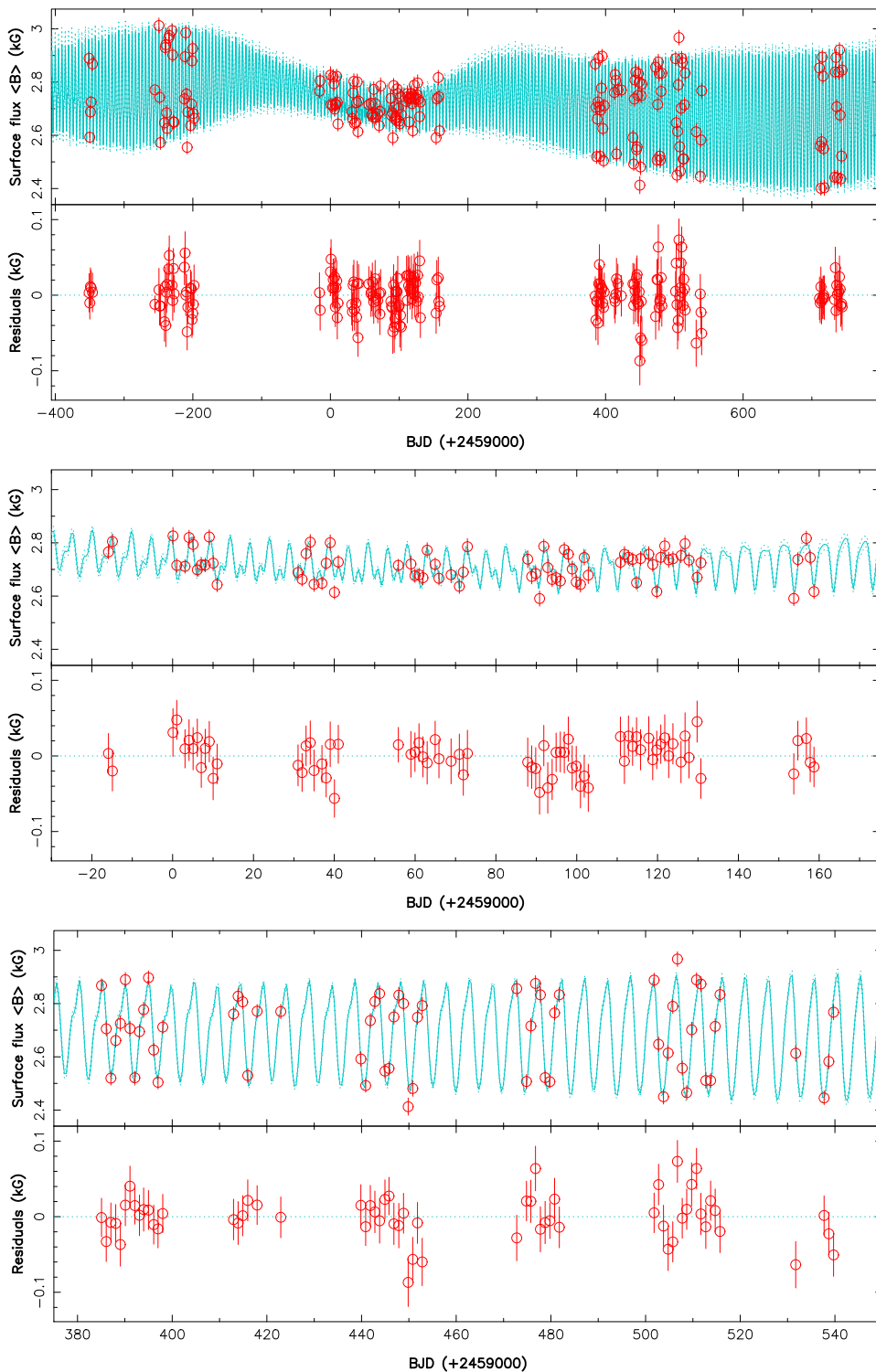


Figure 3. Same as Fig. 2 for the small-scale magnetic flux $\langle B \rangle$ at the surface of AU Mic. The RMS of the residuals is 0.02 kG, yielding $\chi_r^2 = 0.78$, whereas the χ_r^2 with respect to the weighted average is 22.4.

inhomogeneities (in agreement with the small amplitude of photometric variations, of order of a few per cent). For instance, the Doppler width of the local profile v_D that is needed to reproduce the average Stokes I profile of AU Mic with minimal Zeeman broadening is found to be $v_D = 5.3 \text{ km s}^{-1}$ (assuming $v \sin i = 8.5 \text{ km s}^{-1}$, see Section 3), whereas this parameter is typically equal to $v_D \simeq 3 \text{ km s}^{-1}$

for weakly active, slowly rotating M dwarfs of similar spectral type. The large difference in FWHM between the average Stokes I and LSD profiles associated with high-Landé and low-Landé lines (see Section 4) further confirms that this excess broadening is mostly of magnetic origin. In practice, we find that the Stokes I and V profiles of AU Mic can be entirely explained by magnetic field variations

at the surface of the star. Consistently reproducing the FWHMs of the Stokes *I* LSD profiles associated with high-Landé and low-Landé lines for small-scale fields of about 2.5 kG (see Section 4 and Kochukhov & Reiners 2020) requires setting $v_D = 3.5 \text{ km s}^{-1}$, on the high side of what is observed for weakly active M dwarfs.

Given this, we chose to carry-out 2 different sets of complementary magnetic reconstructions. We first focus on Stokes *V* LSD profiles only and assume $v_D = 5.3 \text{ km s}^{-1}$, i.e. the Doppler width of the local profile that enables to reproduce Stokes *I* LSD profiles with minimal Zeeman broadening. We further assume that only a fraction f_V of each grid cell (called filling factor of the large-scale field, equal for all cells) actually contributes to Stokes *V* profiles, with a magnetic flux over the cells equal to B_V (and thus a magnetic field within the magnetic portion of the cells equal to B_V/f_V). This approach, called ‘Stokes *V* analysis’ below, allows one to model the large-scale field and its temporal evolution over the 3 yr of our observations. It is similar to the study of Klein et al. (2021) in this respect (regarding v_D and f_V in particular), except for simultaneous brightness imaging that has very little impact on the reconstructed magnetic map and that we therefore left out of the process.

In a second step, we model both Stokes *V* and Stokes *I* LSD profiles, this time assuming $v_D = 3.5 \text{ km s}^{-1}$, i.e. the value that yields the observed FWHMs of the Stokes *I* LSD profiles of high-Landé et low-Landé lines when the Zeeman broadening of a $\simeq 2.5 \text{ kG}$ small-scale field is taken into account. This approach, called ‘Stokes *I* & *V* analysis’ below, leads to a significantly stronger reconstructed field (than in the Stokes *V* analysis), which should now be consistent with both the large-scale field constraints provided by Stokes *V* profiles and the small-scale field ones coming from Stokes *I* data. In this case, we further assume that a fraction f_I of each grid cell (called filling factor of the small-scale field, again equal for all cells) hosts small-scale fields of strength B_I/f_I (i.e. with a small-scale magnetic flux over the cell equal to $B_I = B_V/f_V/f_I$). This simple model implies in particular that the small-scale field locally scales up with the large-scale field (with a scaling factor of f_I/f_V), which is likely no more than a rough approximation. That the small-scale field is modulated with rotation (see Section 4) actually suggests that it may indeed spatially correlate with the large-scale field to some degree. In practice, we carried out ZDI for various values of f_I and f_V , and selected the pair that fits the data best. In both cases, we assumed $i = 80^\circ$ for the inclination of the rotation axis to the line of sight, i.e. slightly lower than the inclination of the orbital planes of planets b and c (see Table 1), to reduce mirroring effects of the imaging process between the upper and lower hemispheres.

Both methods have their own pros and cons. The Stokes *V* analysis makes it possible to optimally fit the Stokes *V* profiles, yielding the minimal large-scale field (and variations with time) required by the data, but is not able to account for the observed small-scale field. It is well adapted to investigate the temporal evolution of the large-scale field, either from season to season, or under the effect of surface differential rotation (DR) within a given season. The Stokes *I* & *V* analysis is better suited to study the small-scale field and presumably yields a more accurate estimate of the large-scale field as well, but is less optimal to monitor its temporal changes. We did not attempt to model low-level brightness inhomogeneities whose impact on the Stokes *I* and *V* profiles is quite small, nor to model changes in the Stokes *I* profiles caused by magnetic fields with pseudo-brightness features inducing similar profile distortions (as done in Klein et al. 2021). We report the results of both approaches in Sections 5.2 and 5.3.

Finally, we also looked for signatures of DR at the surface of the star, in the same way as in previous studies, i.e. by assuming a 2-

parameter DR law similar to that of the Sun, with the rotation rate at latitude θ being given by $\Omega(\theta) = \Omega_{\text{eq}} - d\Omega \sin^2 \theta$, where Ω_{eq} , and $d\Omega$, respectively stand for the rotation rate at the equator and the difference in rotation rate between the equator and the pole. We then look for the pair of DR parameters that provides the best fit to the data at given image information content. To ensure maximum sensitivity, we concentrate on Stokes *V* data only that are best suited for diagnosing temporal variability of the large-scale field. Results are reported in Section 5.4.

Since the time-scale on which the large-scale field of AU Mic evolves ($\simeq 80 \text{ d}$, see Section 4) is much shorter than our overall observing window of 3 yr, we chose to divide our data set into 4 different subsets, each more or less corresponding to one of our observing season (2019 September–November, 2020 April–November, 2021 June–November, 2022 May–June) containing respectively 28, 78, 65, and 20 spectra, and covering time slots of 57, 175, 155, and 33 d (about 12, 36, 32, and 7 rotation cycles), i.e. 0.4 to $2.2 \times$ the evolution time-scale of the longitudinal magnetic field θ_3 (80 d, see Section 4). The median time shifts between these 4 successive seasons, equal to 298, 391, and 265 d (about 61, 80, and 55 rotation cycles), are $3.3\text{--}4.9 \times$ larger than θ_3 . The few spectra collected early in 2019 April and June (at 6 main epochs, see Table A1), not providing enough phase coverage by themselves, were excluded from this analysis.

Images shown in Sections 5.2 and 5.3 are derived with DR parameters of $\Omega_{\text{eq}} = 1.299 \text{ rad d}^{-1}$ and $d\Omega = 0.037 \text{ rad d}^{-1}$, an average of the values we infer from our 2020 and 2021 data sets (see Section 5.4).

5.2 Stokes *V* analysis of LSD profiles

The sets of Stokes *V* LSD profiles collected with SPIRou for the 4 main seasons outlined previously, along with the ZDI fit to the data (assuming $v_D = 5.3 \text{ km s}^{-1}$ for the Doppler width of the local profile), are presented in Fig. B1 (as supplementary material), whereas the corresponding reconstructed images are shown in Fig. 4. As in Klein et al. (2021), we find that $f_V \simeq 0.2$ provides the best fit to the data for all epochs. Error bars of Stokes *V* LSD profiles (see Table A1) had to be increased by 40–60 per cent for ZDI to be able to reach a unit χ_r^2 , as with B_ℓ for which GPR also diagnosed the presence of additional uncorrelated noise (see Section 4). The required increase in error bars is larger for our 2 longest seasons (2020 and 2021) and smaller for the shortest ones (2019 and 2022), further confirming that it likely reflects intrinsic variability from the intense activity of AU Mic.

Taking into account the phase shift mentioned in Section 3, our 2019 magnetic image resembles that of Klein et al. (2021), with a radial magnetic field reaching 700 G at phase 0.6 (phase 0.2 in Klein et al. 2021) at mid-latitudes, along with consistent patches of azimuthal field of different polarities. Although both studies use the same data (except for one low-SNR observation, marked with an ‘x’ in Table A1, left out from the first analysis and whose impact on the reconstructed image is insignificant), the two images are not exactly identical, the new one being reconstructed for a slightly larger $v \sin i$ (8.5 km s^{-1} instead of 7.8 km s^{-1}) and a different pair of DR parameters (see Section 5.4). As a result, the field we reconstruct is slightly smaller than (though still consistent with) that of Klein et al. (2021), with a quadratically averaged large-scale magnetic flux over the stellar surface equal to $\langle B_V \rangle \simeq 380 \text{ G}$. The large-scale field is mostly poloidal and axisymmetric, with the poloidal component enclosing 75 per cent of the reconstructed field energy, 75 per cent of which in axisymmetric modes. The dipole component reaches a

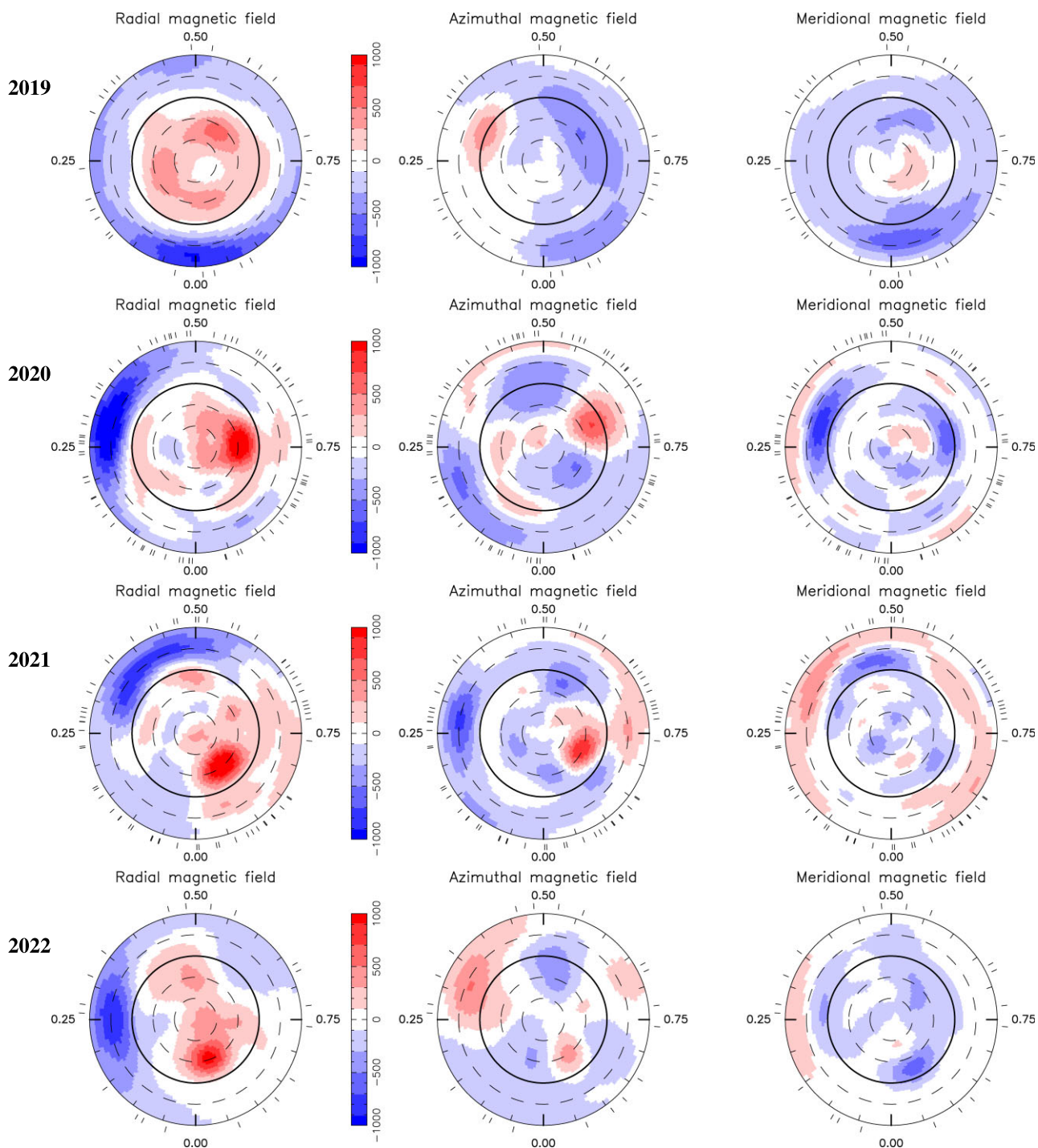


Figure 4. Reconstructed maps of the large-scale field of AU Mic (left, middle, and right columns for the radial, azimuthal and meridional components in spherical coordinates, in G), for season 2019 September–November, 2020 April–November, 2021 June–November and 2022 May–June (top to bottom row, respectively), derived from the Stokes V LSD profiles of Fig. B1 using ZDI (see Section 5.2). The maps are shown in a flattened polar projection down to latitude -60° , with the north pole at the centre and the equator depicted as a bold line. Outer ticks indicate phases of observations. Positive radial, azimuthal, and meridional fields respectively point outwards, counterclockwise and polewards. Each image shows the evolving magnetic map (as a result of DR) at mid-time throughout the season.

strength of $B_d = 430$ G at the pole, and is inclined at 15° to the rotation axis towards phase 0.65.

The 2020 and 2021 images are reconstructed from data sets covering a $3 \times$ longer time span and are thus much better constrained, especially regarding DR (see Section 5.4). Again, we find that

AU Mic hosts a dominantly poloidal large-scale field enclosing 85 percent of the reconstructed energy (of which 35 percent in axisymmetric modes), and that $\langle B_V \rangle$ ranges from 360 G (in 2021) to 400 G (in 2020). Both magnetic maps feature a strong positive radial field region at a latitude of 30° (at phases 0.73 in 2020 and

0.91 in 2021) where B_V reaches 1.2 kG, and another similar one of opposite polarity in the other hemisphere, located more or less symmetrically from the positive one with respect to the centre of the star. These radial field regions are accompanied by an azimuthal field region of identical polarity, located at a similar latitude and a slightly smaller phase. Apart from a global phase shift (of 0.17 cycle) that likely reflects the effect of DR at a latitude of $\approx 30^\circ$ over the time span that separates both data sets (equal to 80 rotation cycles of AU Mic), the 2020 and 2021 magnetic maps share obvious similarities, featuring dipole components of $B_d = 440$ and 400 G, respectively tilted at 40° and 50° to the rotation axis (towards phase 0.75 and 0.85). Despite this resemblance, the detailed maps depart enough from one another to generate B_ℓ curves that are significantly different, as a result of temporal evolution (on a timescale of 80 d, see Section 4 and Fig. 2).

Although derived from the sparsest of our 4 data sets, the 2022 magnetic image of AU Mic is largely similar to the previous ones, with a 1 kG positive radial field region reconstructed at mid latitude (phase 0.96), but with the main negative radial field region no longer showing up at the antipodes of the positive one. The azimuthal field regions accompanying the radial field ones are also much weaker than in the previous 2 images. We find that $\langle B_V \rangle$, equal to 330 G, is weaker than in the previous seasons, and so is the dipole component $B_d = 380$ G (tilted at 35° towards phase 0.80). Once more, the poloidal component largely dominates the large-scale field topology, enclosing 90 per cent of the reconstructed magnetic energy, 45 per cent of which in axisymmetric modes.

All properties of the reconstructed large-scale magnetic field are summarized in Table 3 for our 4 observing seasons.

5.3 Stokes I & V analysis of LSD profiles

We now analyse Stokes I and V LSD profiles together, setting now $v_D = 3.5 \text{ km s}^{-1}$ for the Doppler width of the local profile. It allows us to infer constraints on the small-scale and large-scale magnetic fields B_I and B_V simultaneously, under the assumption that the first scales up with the second with a fixed factor of f_I/f_V (see Section 5.1). In practice, we find that $f_I = 0.9$ provides good results, in rough agreement with the results of Section 3, implying a scaling factor of the small-scale to large-scale field equal to $f_I/f_V = 4.5$. This is also consistent with previous results, indicating that active M dwarfs like AU Mic are able to trigger large-scale fields $\langle B_V \rangle$ whose strength reaches up to 30 per cent that of small-scale fields $\langle B_I \rangle$ (Morin et al. 2010; Kochukhov 2021).

With this approach, we find that the large-scale field of AU Mic is significantly stronger than that derived in Section 5.2, including in particular a more intense, mostly axisymmetric, dipole component. This is consistent with the small-scale field $\langle B \rangle$ directly measured from magnetically sensitive lines, and from the observed differential broadening between the high-Landé and low-Landé Stokes I LSD profiles. Since small-scale fields are assumed to scale up with large-scale fields in our simple model, ZDI has no other choice than increasing the large-scale field as well to generate the adequate level of magnetic broadening in the Stokes I LSD profiles. Despite this additional constraint, ZDI is still able to fit the Stokes V LSD profiles at the same time as the Stokes I LSD profiles, adding to the large-scale field a nearly axisymmetric dipole component that contributes no more than marginally to the Stokes V profiles (as a result of the geometrical configuration, with the star being close to equator-on for an Earth-based observer).

The properties of the reconstructed magnetic fields are summarized in columns 6 to 10 of Table 3 for our 4 seasons. In average, we

find that $\langle B_V \rangle$ now reaches fluxes of 520–570 G, i.e. $1.5\times$ larger than when fitting Stokes V LSD profiles only. It implies small-scale field fluxes of $\langle B_I \rangle = 2.3\text{--}2.6 \text{ kG}$, in agreement with the results of Sections 3 and 4, as well as with those of Kochukhov & Reiners (2020). The difference with the results of Section 5.2 also shows up on the inferred dipole component, now $1.6\times$ larger than in the Stokes V -only reconstruction, with the poloidal component enclosing 75–90 per cent of the reconstructed magnetic energy. As the added dipole is mostly axisymmetric, the tilt of the overall dipole component to the rotation axis is smaller ($10\text{--}25^\circ$) and the poloidal component is mostly axisymmetric (75–90 per cent in terms of magnetic energy). We show one example reconstruction for season 2020 in Fig. 5, the inferred maps for the 3 other seasons looking similar.

We stress that, although our new set of magnetic maps are able to fit both Stokes I and V data, they may still not match the real ones as the imaging problem is ill-posed. This is especially true for AU Mic, whose almost equator-on orientation and small $v \sin i$ both contribute to the problem degeneracy. For instance, adding small-scale tangled fields more or less evenly at the surface of AU Mic without modifying the large-scale field reconstructed from Stokes V profiles only, may also provide a comparable fit to the Stokes I and V profiles, but with a magnetic topology that does not have a fixed amount of small-scale to large-scale field ratio over the surface. This second model would however generate very little rotational modulation of the small-scale field, thereby contradicting our $\langle B \rangle$ measurements from magnetically sensitive lines (see Section 4). Further constraining the imaging process would require collecting LSD profiles for Stokes Q and U LSD profiles, in addition to Stokes V and I profiles, as previously suggested by Kochukhov & Reiners (2020). Fig. C1 (provided as supplementary material) shows for instance that Stokes Q and U signatures (not measured in our campaign) would be detectable and allow one to unambiguously differentiate between the maps of Sections 5.2 and 5.3.

5.4 Differential rotation from Stokes V LSD profiles

Last but not the least, one can study the amount of latitudinal DR shearing the surface of AU Mic from the recurrence periods of the Stokes V signatures associated with the magnetic features reconstructed at different latitudes. As the goal is to diagnose subtle evolution of the Stokes V signatures with time, the most reliable approach is to focus on Stokes V LSD profiles only (as in Section 5.2), even though the large-scale field itself may actually be stronger than what Stokes V LSD profiles alone indicate (see Section 5.3). As outlined in Section 5.1, this is achieved by reconstructing magnetic maps at given information content (i.e. at given magnetic energy) over a given grid of DR parameters. We then fit the resulting χ_r^2 map with a 2D paraboloid, the location of the minimum and the paraboloid curvature at this location respectively providing the optimal DR parameters and the associated error bars (Donati, Collier Cameron & Petit 2003).

We first find that data sets corresponding to seasons 2019 and 2022 do not span long enough a time slot and include too few profiles to yield reliable DR estimates, especially for a star like AU Mic whose $v \sin i$ is on the low side, and that exhibits a high level of intrinsic variability, even on its large-scale field (see Section 4). More specifically, we find that the derived χ^2 maps for both epochs are noisy, showing low-level fluctuations with no obvious minimum over the grid of DR parameters, possibly as a result of short-term intrinsic variability distorting magnetic maps and preventing the DR signal to build-up in a consistent way. For season 2019 and with the same data, Klein et al. (2021) were able to locate a minimum

Table 3. Properties of the large-scale (columns 2 to 6 and 8 to 10) and small-scale (column 7) magnetic field of AU Mic for our 4 observing seasons. Columns 2 to 5 correspond to the ZDI Stokes V analysis (assuming $f_V = 0.2$ and $v_D = 5.3 \text{ km s}^{-1}$, see Section 5.2), whereas columns 6 to 10 summarize the results of the ZDI Stokes I & V analysis (assuming $f_I = 0.9$, $f_V = 0.2$ and $v_D = 3.5 \text{ km s}^{-1}$, see Section 5.3). Columns 3 and 8 list the polar strengths of the dipole component B_d , columns 4 and 9 the tilts of the dipole component to the rotation axis, and columns 5 and 10 the amount of magnetic energy reconstructed in the poloidal component of the field and in the axisymmetric modes of this component. Error bars on field values and percentages are typically equal to 5–10 per cent.

Season	Stokes V analysis ($f_V = 0.2, v_D = 5.3 \text{ km s}^{-1}$)				Stokes I & V analysis ($f_I = 0.9, f_V = 0.2, v_D = 3.5 \text{ km s}^{-1}$)				
	$\langle B_V \rangle$ (G)	B_d (G)	tilt ($^\circ$)	poloidal/axisym (%)	$\langle B_V \rangle$ (G)	$\langle B_I \rangle$ (kG)	B_d (G)	tilt ($^\circ$)	poloidal/axisym (%)
2019 Sep–Nov	380	430	15	75/75	550	2.5	650	10	85/90
2020 Apr–Nov	400	440	40	85/35	570	2.6	660	25	90/75
2021 Jun–Nov	360	400	50	85/35	530	2.4	650	25	90/75
2022 May–Jun	330	380	35	90/45	520	2.3	660	20	90/80

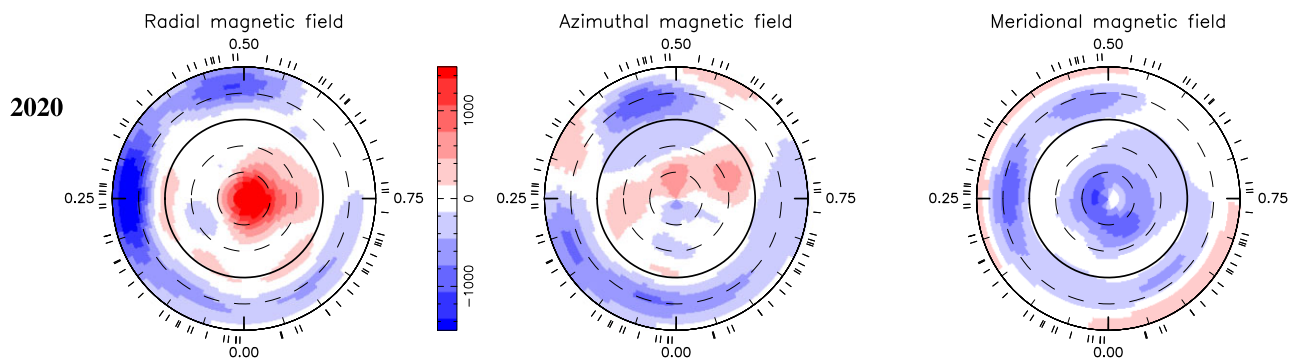


Figure 5. Same as the second top row of Fig. 4 (2020 April–November), with the field now reconstructed using both Stokes I & V LSD profiles (see Section 5.3). Note the different colour scale to depict magnetic fluxes.

in the χ_r^2 map outside our grid of DR parameters, corresponding to an unexpectedly strong DR for an M dwarf like AU Mic. We thus suspect this early estimate to rather reflect the impact of intrinsic variability rather than the shearing effect of DR.

The data sets we collected over the 2020 and 2021 seasons, respectively spanning 36 and 32 rotation cycles and gathering 78 and 65 Stokes V LSD profiles, are much better suited for deriving reliable DR estimates. We find that $\Omega_{\text{eq}} = 1.3006 \pm 0.0004 \text{ rad d}^{-1}$ and $d\Omega = 0.0445 \pm 0.0014 \text{ rad d}^{-1}$ for season 2020, and $\Omega_{\text{eq}} = 1.2970 \pm 0.0002 \text{ rad d}^{-1}$ and $d\Omega = 0.0298 \pm 0.0013 \text{ rad d}^{-1}$ for season 2021, with the two estimates differing by more than 3σ between both epochs suggesting that DR may be varying at the surface of AU Mic (see Fig. 6), on a time-scale similar to that on which the large-scale field evolves. We however note that the error bars on DR parameters are bigger in 2020 than in 2021 despite the larger number of points in the data set and the similar reconstructed magnetic images (see Fig. 4). We suspect that it again reflects the impact of intrinsic variability (e.g. from stochastic changes of the magnetic maps), that happened to be larger in 2020 than in 2021 judging from the decay time and residuals inferred by GPR from the B_ℓ data (see Section 4 and Fig. 2), and which presumably broadened the 2D χ_r^2 paraboloid in 2020 more than in 2021. Splitting the data set of each season into 2 subsets and carrying out the same process on each subset indeed yields noisy χ_r^2 maps and discrepant DR parameters, consistent with our previous conclusion that extensive observations collected over a full season are needed to obtain a reliable DR measurement.

Given that DR measurements of AU Mic are apparently quite sensitive to intrinsic variability, the difference between the values

inferred from our 2020 and 2021 Stokes V data may not be so significant, despite their differing by more than 3σ . This is why all magnetic images presented in Sections 5.2 and 5.3 were derived using average DR parameters from both seasons (i.e. $\Omega_{\text{eq}} = 1.299 \text{ rad d}^{-1}$ and $d\Omega = 0.037 \text{ rad d}^{-1}$). These average parameters imply that the equator of AU Mic rotates in about 4.84 d whereas its pole rotates in about 4.98 d, with a typical timescale of 170 d for the equator to lap the pole by one complete cycle. This timescale is about twice longer than the evolution timescale derived from the GP fit to the B_ℓ data (see Table 1), indicating that DR itself is likely not the main contributor to the overall large-scale field distortion with time.

In this context, the nominal period of AU Mic (of 4.86 d, used to phase our data, see Table 1) corresponds to a latitude of 24° whereas that derived from the GP fit to the B_ℓ data ($4.856 \pm 0.003 \text{ d}$) corresponds to latitudes in the range 20 – 24° , and that derived from the GP fit of the $\langle B \rangle$ data ($4.859 \pm 0.004 \text{ d}$) corresponds to latitudes in the range 22 – 26° . Similarly, the phase shift of surface features at latitude 30° over a time-scale of 391 d (i.e. the time shift between seasons 2020 and 2021) is expected to be $+0.19$, slightly larger than, though still comparable to, the observed phase drift of the main radial and azimuthal field features reconstructed at at both epochs at this latitude (of order $+0.15$, see middle rows of Fig. 4).

6 THE MULTIPLANET SYSTEM OF AU MIC

We analysed the 185 RV points derived by the LBL technique (Artigau et al. 2022) from our nightly observations of AU Mic (see Table A1), looking for the RV signatures of the 2 known transiting warm Neptunes hiding within the dominant activity signal modulated

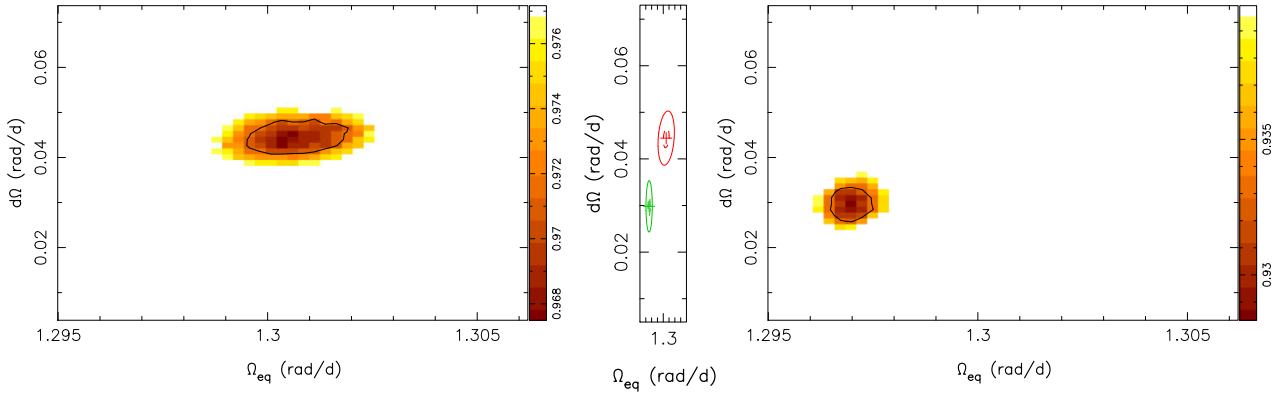


Figure 6. Measuring DR at the surface of AU Mic by minimizing the χ_r^2 of the ZDI fit to our Stokes V LSD profiles over a grid of DR parameters (see Section 5.4), for season 2020 April–November (left-hand panel) and 2021 June–November (right-hand panel). In both panels, the black contour depicts the 3σ confidence interval for the pair of DR parameters. The central panel shows the 1σ and 3σ confidence ellipses for both seasons (in red for 2020 and green for 2021) together on the same plot.

by the rotation period. Our rich data set also allows us to investigate potential RV signatures of additional planets in the AU Mic system, either more distant ones that may not be transiting, or small inner ones like the candidate Earth-mass planet (dubbed d) recently proposed by Wittrock et al. (2023), potentially located between b and c and putatively causing the large TTVs reported for both (Szabó et al. 2022). For planets b and c, the orbital periods and transit times are known with high precision (see Table 4), leaving us with the RV semi-amplitude K_b and K_c to be determined (assuming circular orbits, consistent with the results of Zicher et al. 2022). For candidate planet d, also assumed to be on a circular orbit, we choose the most likely solution of Wittrock et al. (2023), associated with a period of 12.7381 ± 0.0013 d and a conjunction BJD of 2458333.32 ± 0.36 d (both parameters fixed in our modelling), which leaves us with only K_d to be adjusted. For each additional planet to be considered, it adds 3 more free parameters to the problem, the orbital period P_i , the RV semi-amplitude K_i and the date of conjunction BJD $_i$ (assuming again circular orbits). Although TTVs are quite significant for the actual transits of b and c (Szabó et al. 2022), we do not take them into account in our RV modelling, as they still correspond to very small phase shifts (of about 0.3 per cent of an orbital cycle for the innermost planet). The default transit times and orbital periods that we use for planets b and c in our analysis are those of Szabó et al. (2022) that minimize the amplitude of TTVs over all transits observed so far.

In practice, we use a GPR with a QP kernel to model activity, coupled to a MCMC process to determine the posterior distributions of the planet parameters and of the GP hyper parameters. We run different joint models, one featuring planets b and c only which we take as a reference, plus others, either without b and c, or with additional planets whose RV signatures may also be present in the data. The marginal logarithmic likelihood $\log \mathcal{L}_M$ of a given solution is computed using the approach of Chib & Jeliazkov (2001) as described in Haywood et al. (2014), and the significance of the RV signatures of additional non-transiting planets is estimated from the difference in $\log \mathcal{L}_M$ (i.e. the logarithmic Bayes Factor $\log \text{BF}$) with respect to our reference model.

When including planets b and c only, we derive similar semi-amplitudes for their RV signatures, equal to $K_b = 4.1^{+1.8}_{-1.2} \text{ m s}^{-1}$ and $K_c = 4.0^{+1.7}_{-1.2} \text{ m s}^{-1}$ (see Table 4 and Fig. 7), less than the estimates published earlier but none the less consistent within about 2σ (Cale et al. 2021; Klein et al. 2021; Zicher et al. 2022). The RV signatures of both planets show up at a level of 3.4σ . The GP amplitude

reaches $30 \pm 4 \text{ m s}^{-1}$, about $7\times$ larger than the semi-amplitudes of the planet signatures, stressing how intense activity is in the case of as young a star as AU Mic. Besides, the RMS of the fit to our RV data is equal to 11.1 m s^{-1} , $2.9\times$ larger than the median error bar of our RV measurements (3.8 m s^{-1} , see Table A1), a likely result of a high level of activity-induced intrinsic variability and of potential RV signatures of additional system planets not yet included in the analysis. This illustrates how tricky the detection of planet RV signatures can be for very active stars, even in the case of transiting planets whose orbital periods and transit times are well documented from high-precision photometry, and how efficient activity filtering needs to be to reliably unveil planet RV signatures. When including planets b and c and compared to a model with no planet, we find that $\log \mathcal{L}_M$ increases by 6.3 while the dispersion of RV residuals and the additional white noise parameter θ_5 both decrease (see Table 4), confirming that adding both planets provides a more reliable description of our RV data. Adjusting the eccentricity of planets b and c along with the other parameters yields no more than a small improvement ($\Delta \log \mathcal{L}_M = 0.3$) and eccentricities compatible with 0 (with error bars of 0.04 and 0.08 for planets b and c), consistent with the results of Zicher et al. (2022) and justifying our a priori assumption of circular orbits³.

We explored the possibility of an additional system planet whose RV signatures would still be hiding in our data. By looking at the periodogram of the filtered RV data, we find residual power at a period of 33.4 d that may hint at the presence of a candidate planet (dubbed planet e), which would be located further out close to a 4:1 resonance with planet b and 7:1 resonance with the rotation period of the host star. When candidate planet e is taken into account in the modelling and MCMC searches again for the most likely combination of activity and planet signatures, the 33.4 d peak dominates the periodogram of the filtered RVs at a level that corresponds to a false alarm probability (FAP) that the signal is spurious of order 10^{-10} . We find an orbital period of $P_e = 33.39 \pm 0.10$ d and a semi-amplitude of $K_e = 11.1^{+2.1}_{-1.7} \text{ m s}^{-1}$ for candidate planet e, i.e. about $2.5\times$ larger than those of planets b and c. The RV signal is detected at a level of

³We adjust eccentricities using variables $\sqrt{e} \cos \omega$ and $\sqrt{e} \sin \omega$ (e being the eccentricity and ω the angle of periastron) and Gaussian priors (0.0, 0.3) for both, in agreement with the observed distribution of eccentricities for multi-planet systems (Van Eylen et al. 2019).

Table 4. MCMC results for the 4 studied cases (no planet, b + c, b + c + e, b + c + e + d). For each case, we list the recovered GP and planet parameters with their error bars, as well as the priors used whenever relevant. The last 4 rows give the χ_r^2 and the RMS of the best fit to our RV data, as well as the associated marginal logarithmic likelihood $\log \mathcal{L}_M$ and marginal logarithmic likelihood variation $\Delta \log \mathcal{L}_M$ with respect to the reference case (b + c).

Parameter	No planet	b + c	b + c + e	b + c + e + d	Prior
θ_1 (m s ⁻¹)	30.1 ^{+3.9} _{-3.4}	30.3 ^{+3.9} _{-3.5}	31.6 ^{+4.7} _{-4.1}	31.5 ^{+4.7} _{-4.1}	mod Jeffreys (σ_{RV})
θ_2 (d)	4.865 ± 0.005	4.863 ± 0.006	4.865 ± 0.005	4.865 ± 0.005	Gaussian (4.86, 0.1)
θ_3 (d)	139 ⁺²³ ₋₂₀	136 ⁺²³ ₋₂₀	136 ⁺²² ₋₁₉	136 ⁺²² ₋₁₉	log Gaussian (log 140, log 1.5)
θ_4	0.29 ± 0.04	0.29 ± 0.04	0.37 ± 0.06	0.37 ± 0.06	Uniform (0, 3)
θ_5 (m s ⁻¹)	14.2 ± 1.0	13.5 ± 1.0	12.5 ± 0.9	12.7 ± 0.9	mod Jeffreys (σ_{RV})
K_b (m s ⁻¹)		4.1 ^{+1.8} _{-1.2}	4.5 ^{+1.7} _{-1.2}	4.6 ^{+1.7} _{-1.2}	mod Jeffreys (σ_{RV})
P_b (d)		8.4631427	8.4631427	8.4631427	fixed from Szabó et al. (2022)
BJD _b (2459000 +)		-669.61584	-669.61584	-669.61584	fixed from Szabó et al. (2022)
M_b (M _⊕)		9.3 ^{+4.1} _{-2.7}	10.2 ^{+3.9} _{-2.7}	10.4 ^{+3.9} _{-2.7}	derived from K_b , P_b and M_*
K_c (m s ⁻¹)		4.0 ^{+1.7} _{-1.2}	4.8 ^{+1.6} _{-1.2}	5.1 ^{+1.6} _{-1.2}	mod Jeffreys (σ_{RV})
P_c (d)		18.85882	18.85882	18.85882	fixed from Szabó et al. (2022)
BJD _c (2459000 +)		454.8973	454.8973	454.8973	fixed from Szabó et al. (2022)
M_c (M _⊕)		11.8 ^{+5.1} _{-3.5}	14.2 ^{+4.8} _{-3.5}	15.1 ^{+4.8} _{-3.5}	derived from K_c , P_c and M_*
K_e (m s ⁻¹)			11.1 ^{+2.1} _{-1.7}	11.3 ^{+2.2} _{-1.8}	mod Jeffreys (σ_{RV})
P_e (d)			33.39 ± 0.10	33.39 ± 0.10	Gaussian (33.4, 1.0)
BJD _e (2459000 +)			117.1 ± 0.9	117.1 ± 0.9	Gaussian (118, 8)
M_e (M _⊕)			35.2 ^{+6.7} _{-5.4}	35.9 ^{+6.9} _{-5.8}	derived from K_e , P_e and M_*
K_d (m s ⁻¹)				1.1 ^{+1.1} _{-0.5}	mod Jeffreys (σ_{RV})
P_d (d)				12.73812	fixed from Wittrock et al. (2023)
BJD _d (2459000 +)				-666.6789	fixed from Wittrock et al. (2023)
M_d (M _⊕)				2.9 ^{+2.9} _{-1.3}	derived from K_d , P_d and M_*
χ_r^2	10.4	9.8	8.5	8.5	
RMS (m s ⁻¹)	11.5	11.1	10.4	10.4	
$\log \mathcal{L}_M$	458.8	465.1	481.4	481.7	
$\log \text{BF} = \Delta \log \mathcal{L}_M$	-6.3	0.0	16.3	16.6	

6.5 σ , with $\log \mathcal{L}_M$ increasing by 16.3 with respect to the reference case with planets b and c only, and the RMS of the RV residuals and the additional white noise θ_5 both decreasing. With this model, the semi-amplitudes associated with planets b and c slightly increase, reaching now $K_b = 4.5^{+1.7}_{-1.2}$ m s⁻¹ and $K_c = 4.8^{+1.6}_{-1.2}$ m s⁻¹, implying a $\simeq 4\sigma$ detection. The corresponding fit and periodogram are shown in Figs 8 and 9, whereas the phase-folded filtered RV data for planets b, c, and e are presented in Fig. 10 (both before and after binning on phase bins of 10 per cent of their orbital cycles). No peak crosses the 10 per cent FAP threshold in the residual RVs (see Fig. 9 bottom plot). We note that the derived period for candidate planet e is close to a 1-yr alias of the synodic Moon period (32.1 d), visible in the periodogram of the window function, see Fig. 9), but distant from it by more than the FWHM of the periodogram peak, ensuring they are distinct. Adjusting eccentricities of all 3 planets yields again values consistent with 0 (error bars of 0.04, 0.07, and 0.09 for planets b, c, and e, respectively) and no more than a small increase in marginal logarithmic likelihood ($\Delta \log \mathcal{L}_M = 0.8$), confirming that the model with circular orbits is enough to describe our RV data.

Although the periodogram of the RV residuals shows no obvious signal, we investigated whether our RV data could suggest the presence of additional planets beside candidate planet e, in particular the candidate planet d suggested by Wittrock et al. (2023) that may orbit between b and c and potentially explain the large TTVs reported for b and c. When including all 4 planets in the modelling (assuming again circular orbits), we find very similar results for b, c, and e (see Table 4), and a very small semi-amplitude of $K_d = 1.1^{+1.1}_{-0.5}$ m s⁻¹, which in fact amounts to a mere 3 σ upper limit on K_d of 4.4 m s⁻¹. As expected, the marginal logarithmic likelihood increases very little ($\Delta \log \mathcal{L}_M = 0.3$) when d is included in the modelling, implying that

our data provide no evidence for its existence (within the quoted 3 σ upper limit).

We finally note that the parameters of the fitted GP are similar for all cases, except for the additional white noise (θ_5) which decreases when adding planets b, c, and e in the model. We find that the time-scale on which the activity jitter evolves is longer than that on which B_ℓ changes but similar to that associated with $\langle B \rangle$. We also obtain that the rotation period derived from the activity jitter ($\theta_2 = 4.865 \pm 0.005$ d) is marginally longer than the nominal one used to phase the data (4.86 d, see Table 1) and those derived from B_ℓ and $\langle B \rangle$ measurements (respectively equal to 4.856 ± 0.003 and 4.859 ± 0.004 d). These periods indicate that the centre of gravity of the surface features generating the activity jitter is located within the range of latitude 25–29° (see Section 5.4). We point out that the smoothing factor θ_4 derived from RV data is smaller than that inferred from B_ℓ and $\langle B \rangle$, as expected from the fact that RV is proportional to the derivative of the integrated flux (at first order), whereas B_ℓ and $\langle B \rangle$ simply grow as the integral of the magnetic field vector/strength over the visible hemisphere. The periodogram of the filtered RVs (see Fig. 9, middle plot) clearly demonstrates that activity filtering using GPR is quite efficient despite the long observing window, with no excess power remaining at the rotation period, harmonics and aliases.

7 ACTIVITY PROXIES OF AU MIC

The main goal of this section is to investigate how the various activity proxies correlate with RVs, to find out whether one can be used to achieve a filtering of the activity jitter that is as accurate as, or even more efficient than, that achieved through GPR (see Section 6).

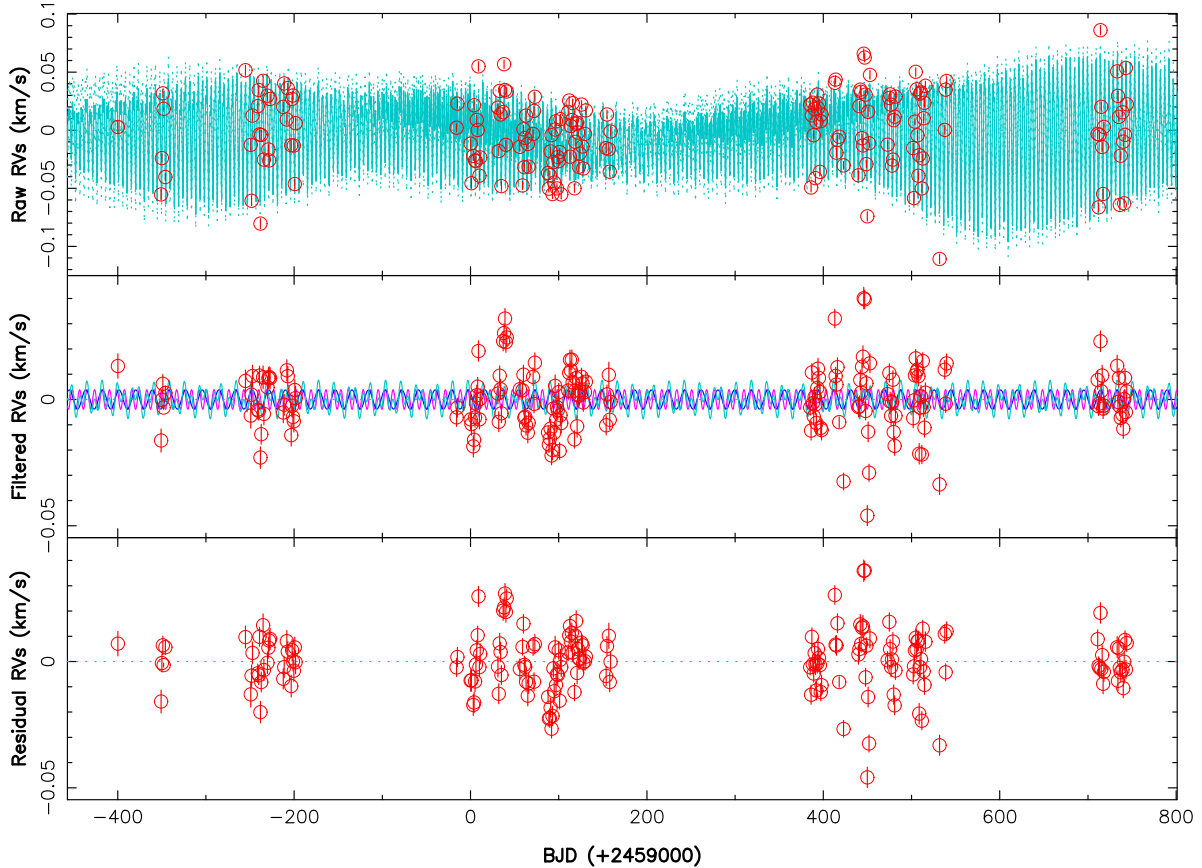


Figure 7. Raw (top), filtered (middle), and residual (bottom) RVs of AU Mic (red dots) over our observing period. The top plot shows the MCMC fit to the data, including a QP GPR modelling of the activity and the RV signatures of planets b and c (cyan), whereas the middle plot shows the planet RV signatures (pink, blue, and cyan for planets b, c and b + c, respectively) once activity is filtered out. The RMS of the residuals is 11.1 m s^{-1} , $2.9\times$ larger than the median error bars (3.8 m s^{-1}) on individual RV points.

The first obvious activity proxy to investigate is the small-scale field $\langle B \rangle$, already studied in Section 4 and reported to correlate well with RVs in the particular case of the Sun (Haywood et al. 2022). We find that RVs of AU Mic correlate poorly with B_ℓ ($R = 0.33$) and $\langle B \rangle$ ($R = 0.12$), but nicely with the first time derivative of $\langle B \rangle$ (computed from the GPR fit to $\langle B \rangle$, $R = 0.78$). This is similar to what was reported by Suárez Mascareño et al. (2020) for Proxima, where RVs are found not to correlate with the FWHM of the cross-correlation profile, presumably linked to $\langle B \rangle$ via magnetic broadening, but with its first time derivative. This is also consistent with our finding that $\langle B \rangle$ correlates reasonably well with the FWHM of the Stokes I profiles of high-Landé lines in AU Mic ($R = 0.60$, see Section 4), but not with what was reported by Klein et al. (2021) in the particular case of the small late-2019 subset (where RVs correlated well with FWHMs). Altogether, it indicates that the activity jitter of M dwarfs like Proxima and AU Mic reflects the RV impact of brightness or magnetic features at the surface of the star, rather than the signature of inhibited convective blue-shift, expected to be much smaller for M dwarfs than for the Sun.

However, trying to directly filter out RVs of AU Mic using the first time derivative of $\langle B \rangle$ as a proxy to predict the activity jitter is less efficient than the GPR filtering outlined in Section 6. We find that the RV residuals are still modulated with rotation, albeit with an amplitude of about 45 percent that of the original jitter. The predicted RV jitter within each season is indeed not entirely consistent with the observed RVs, either in amplitude or in phase

pattern, leaving residuals that still dominate the RV signatures from the 3 planets. Applying the same 3-planet plus QP GPR modeling as that of Section 6 on the filtered RVs yields results for the parameters of b, c, and e and RV residuals that are very similar to those obtained in Section 6. It confirms that the RV signatures detected for all 3 planets are not a spurious artefact induced by activity, but brings no improvement in the RMS of RV residuals. We note that the periodogram of $\langle B \rangle$ only features a strong peak at the rotation period of AU Mic, and virtually no power at the orbital periods of the planets.

Looking now at the LBL activity proxy dLW, we find that it is modulated by rotation, with a QP GPR fit yielding a period of $4.88 \pm 0.03 \text{ d}$, consistent with AU Mic’s reference period of 4.86 d. The dispersion with respect to the fit is $3\times$ larger than the median error bar of individual points (a likely result of intrinsic variability), whereas the modulation amplitude derived by GPR is only 25 percent larger than the dispersion. It is less useful in this respect than $\langle B \rangle$ or even the FWHM of the Stokes I profiles of high-Landé lines, both exhibiting clearer rotational modulation (see Section 4). This difference likely comes from the fact that dLW, computed from all spectral lines (including molecular features, on an average less sensitive to magnetic fields), is less appropriate for diagnosing small-scale magnetic fields than $\langle B \rangle$ or the FWHM of the Stokes I LSD profiles of atomic lines with high Landé factors. We also note that RVs poorly correlate with dLW, as already reported for $\langle B \rangle$ and FWHMs.

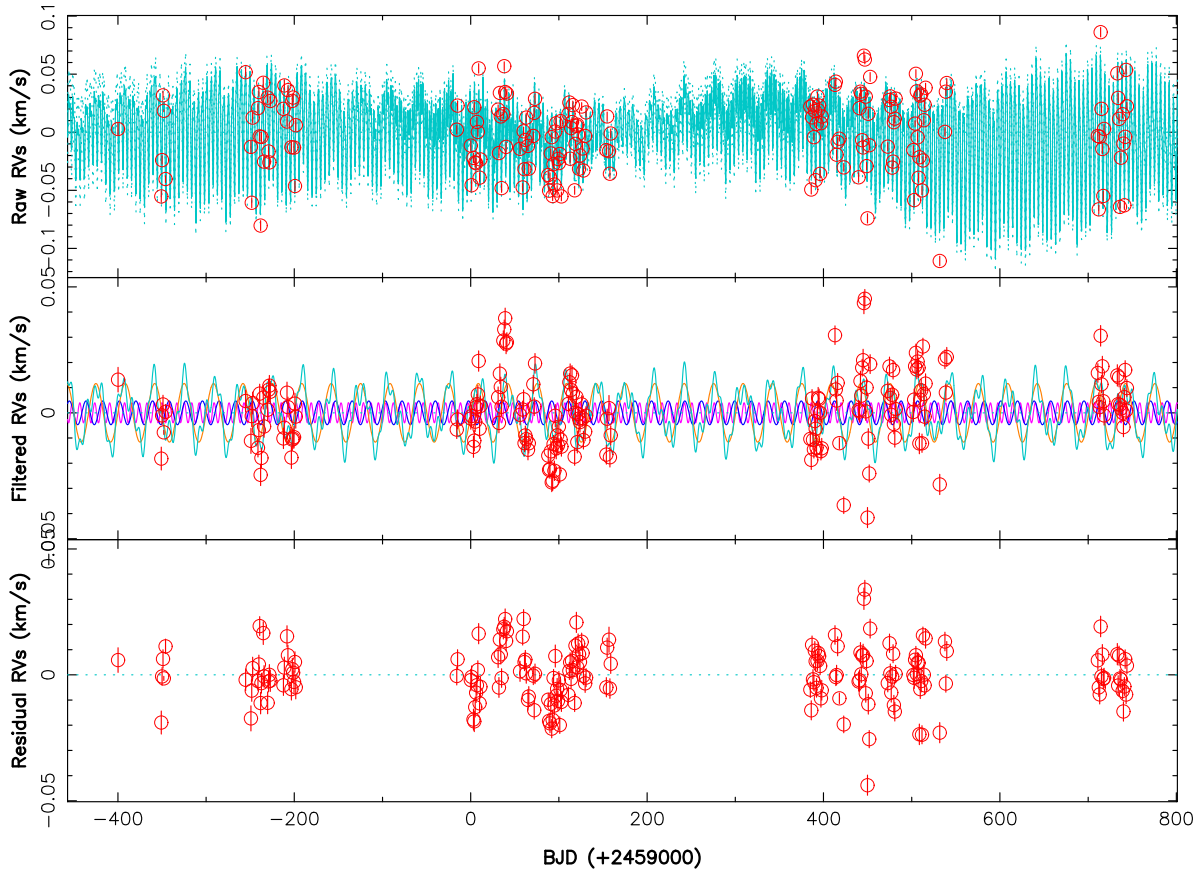


Figure 8. Same as Fig. 7 but including candidate planet e (orange and cyan curves for e and b + c + e in the middle plot) in the MCMC modelling. The RMS of the residuals is now 10.4 m s^{-1} .

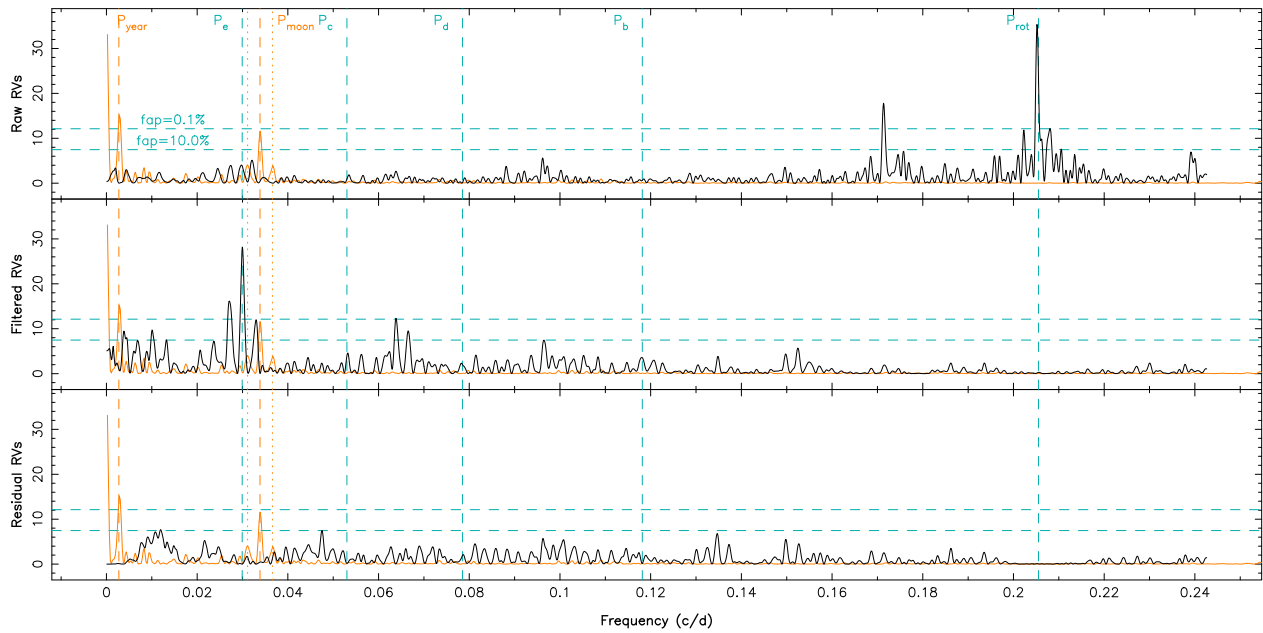


Figure 9. Periodogram of the raw (top), filtered (middle), and residual (bottom) RVs when including candidate planet e (plus b and c) in the MCMC modelling. The cyan vertical dashed lines trace the rotation period of the star and the orbital periods of planets b and c, and of candidate planets d and e, while the horizontal dashed line indicate the 10 and 0.1 per cent FAP levels in the periodogram of our RV data. The orange curve depicts the window function, whereas the orange vertical dashed and dotted line outline the 1-yr period, the synodic period of the Moon and its 1-yr aliases.

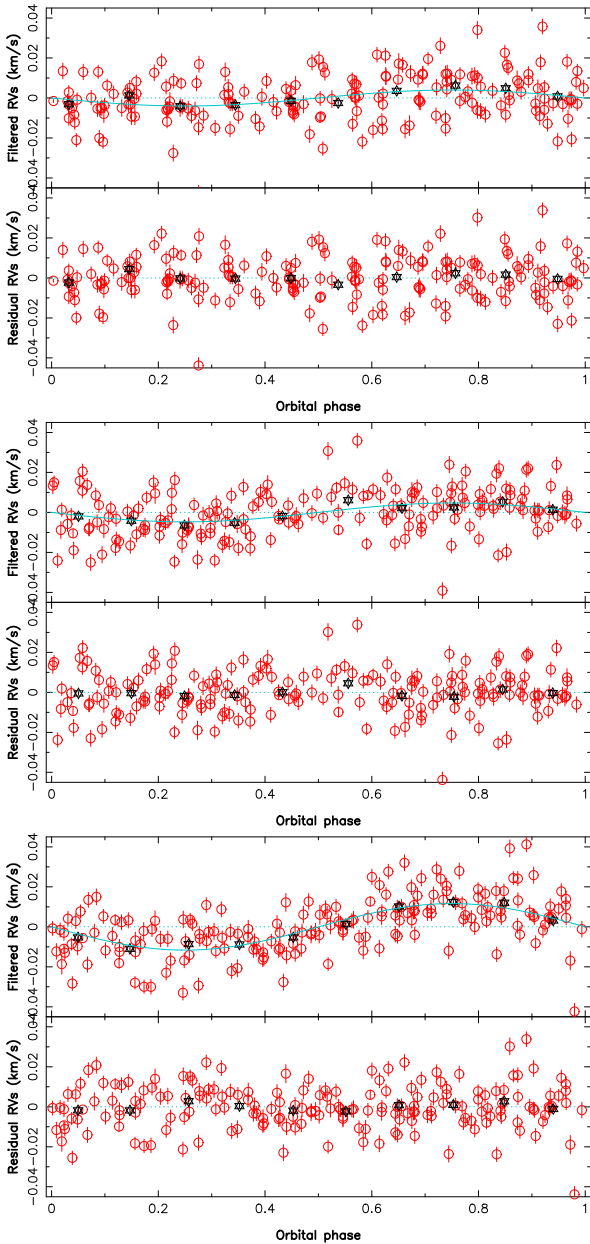


Figure 10. Filtered (top plot) and residual (bottom plot) RVs for transiting planets b (top panel) and c (middle panel), and for candidate planet e (bottom panel) of AU Mic. The red dots are the individual RV points with the respective error bars, whereas the black stars are average RVs over 0.1 phase bins. As in Fig. 8, the dispersion of RV residuals is 10.4 m s^{-1} .

Since dLW is measured on individual lines with LBL, one can carry out a weighted principal component analysis (wPCA; Delchambre 2015) on the time series corresponding to all individual lines, to find out how temporal variations of line widths differ from line to line, as a likely impact of small-scale fields (Cadieux et al. in preparation). When applied to AU Mic, we find that the strongest wPCA component $W_1(t)$ is enough to explain most of the line-to-line differences, and that W_1 is clearly modulated with rotation, with a QP GPR yielding a recurrence period of $4.859 \pm 0.003 \text{ d}$ and a decay time of $141 \pm 15 \text{ d}$, fully consistent with those derived for $\langle B \rangle$ (see lower section of Table 2). Furthermore, we find that W_1 is strongly correlated with $\langle B \rangle$ ($R = 0.96$). Unsurprisingly, using W_1

(instead of $\langle B \rangle$) to filter RVs yields results very similar to those outlined above, i.e. an activity jitter reduced in amplitude by a factor of 2 compared to the original one, but still dominating the planet signatures. The RV planet signatures derived from the filtered RVs are again consistent with the values listed in Table 4.

We also measured equivalent width variations (EWVs) of the 1083 nm He I triplet and 1282 nm Pa β line, tracing stellar activity and potentially star-planet interactions (Klein et al. 2022), and whose profiles are shown in Fig. D1 (supplementary material). We proceeded as in Finocciety et al. (2021, 2023), computing a median spectrum by which all spectra are divided, and fitting a Gaussian profile of fixed width and position (in the stellar rest frame) to the residual spectra. The derived values and error bars are listed in Table A1, with a few flares detected in He I but not in Pa β . We find that both indices are modulated with the stellar rotation period. Fitting the EWVs with GPR yields periods of $4.86 \pm 0.01 \text{ d}$ for both the He I and Pa β lines, when setting the decay time to 100 d (i.e. a value close to that derived from B_t data, see Section 4). In both cases, the excess white noise, quantifying the intrinsic variability of both activity indicators, is significantly larger than the formal photon-noise error bars (median of 0.030 and 0.015 km s^{-1} for He I and Pa β), by an order of magnitude or more, reaching 0.5 and 0.1 km s^{-1} for He I and Pa β . It confirms again the strong variability that AU Mic triggers at all times, especially in the He I line for which the semi-amplitude of the modulation is only about 70 per cent the size of the excess white noise (whereas both are comparable in strength for Pa β). While Pa β EWVs correlate reasonably well with $\langle B \rangle$ ($R = 0.60$), it is not the case for He I EWVs that are much more dispersed, presumably as a result of intrinsic variability and chromospheric activity. We also find that the Pa β EWVs slowly decrease with time like $\langle B \rangle$ does, suggesting that AU Mic may be progressing towards activity minimum along its putative cycle (Ibañez Bustos et al. 2019).

As for $\langle B \rangle$, the periodogram of the Pa β EWVs is featureless apart from the main peak at P_{rot} (with a FAP well below the 0.1 per cent threshold). In particular, no signal shows up at the orbital periods of the planets. The periodogram of the He I EWVs is much more noisy, with again a main peak at P_{rot} (FAP of 0.1 per cent). Multiple peaks are also present at an FAP level of 10 per cent or higher, including at frequencies close to the orbital periods of transiting planets b and c. As these peaks do not correspond to a safe detection, and since similar peaks are also present at different periods throughout the periodogram, we conclude that their proximity with the orbital frequencies of planets b and c is no more than a coincidence.

All activity proxies discussed here exhibit rotational modulation, though with different levels of significance. However, even the best of them, i.e. $\langle B \rangle$ and W_1 (whose first time derivatives correlate well with RVs), are moderately successful at filtering the dominant activity jitter from the RV curve of AU Mic.

8 SUMMARY AND DISCUSSION

Our paper presents a detailed study of the young active star AU Mic based on 235 high-resolution unpolarized and circularly polarized spectra collected with SPIRou at CFHT from early 2019 to mid 2022, covering a timespan of 1144 d over 4 successive seasons.

We revisited the main parameters of AU Mic, including its surface magnetic flux, using the median SPIRou spectrum, and found that $T_{\text{eff}} = 3665 \pm 31 \text{ K}$, $\log g = 4.52 \pm 0.05$, $[M/H] = 0.12 \pm 0.10$ and $[\alpha/\text{Fe}] = 0.00 \pm 0.04$. These parameters are consistent with a mass and radius of $0.60 \pm 0.04 M_{\odot}$ and $0.82 \pm 0.02 R_{\odot}$, respectively, at an age of $\approx 20 \text{ Myr}$, in the context of the Baraffe et al. (2015) and Dotter

et al. (2008) evolutionary models, except for the estimated $\log g$ that is larger (by about 3σ) than that expected from the mass and radius. Given the nominal rotation period of AU Mic (4.86 d), the projected rotation velocity $v \sin i$ is $8.5 \pm 0.2 \text{ km s}^{-1}$, consistent with previous literature estimates. Both evolutionary models further suggest that AU Mic already developed a small radiative core. The small-scale magnetic field $\langle B \rangle$, adjusted with the atmospheric parameters on the median spectrum from a set of nIR lines with known Zeeman patterns (Cristofari et al. 2023), is equal to $2.61 \pm 0.05 \text{ kG}$, again consistent with previous literature measurements and typical to field strengths of active M dwarfs (e.g. Kochukhov & Reiners 2020; Reiners et al. 2022). We find that modelling Zeeman broadening is important to derive accurate atmospheric parameters for strongly magnetic stars like AU Mic.

As in Klein et al. (2021), the large-scale magnetic field of AU Mic is detected through circularly polarized Zeeman signatures of atomic lines. The longitudinal field B_ℓ , probing the large-scale field, exhibits obvious rotational modulation with a period of $4.856 \pm 0.003 \text{ d}$. The corresponding pattern features a semi-amplitude ranging from 100 (in 2019) to 250 G (in 2020) and evolves on a time-scale of $80 \pm 12 \text{ d}$, typical to largely- or fully-convective M dwarfs whose large-scale fields are usually stable over a few months (e.g. Morin et al. 2008a, b; Hébrard et al. 2016). The small-scale field $\langle B \rangle$ also exhibits rotational modulation though weaker than that of B_ℓ , with a different pattern (minimum and maximum amplitude in 2020 and 2021, respectively) and a slightly longer period of $4.859 \pm 0.004 \text{ d}$. The evolution time-scale is about twice longer for $\langle B \rangle$ than for B_ℓ . The FWHM of the Stokes I LSD profiles of atomic lines with high Landé factors comes as an alternate option for measuring $\langle B \rangle$, albeit with a loss of precision.

Applying ZDI on the rotationally modulated sets of LSD Stokes V profiles of each observing season, and setting the Doppler width of the local profile to $v_D = 5.3 \text{ km s}^{-1}$ (to match the shape of the average LSD Stokes I profile with minimal Zeeman broadening), we find that the large-scale field of AU Mic reaches $\simeq 400 \text{ G}$, is mainly poloidal and axisymmetric, and with a dipole component of $\simeq 400 \text{ G}$ tilted at $15\text{--}50^\circ$ with respect to the rotation axis depending on the season. Optimal results are obtained for a filling factor of the large-scale field $f_V \simeq 0.2$. If we include Stokes I LSD profiles in the fitting procedure as well and further assume that the local small-scale field scales up with the local large-scale field (with the filling factor of the small-scale field set to $f_I \simeq 0.9$ and the Doppler width of the local profile to a more conventional value of $v_D = 3.5 \text{ km s}^{-1}$), we find that a stronger large-scale field of $\simeq 550 \text{ G}$ and a small-scale field of $\simeq 2.5 \text{ kG}$ are needed to simultaneously reproduce LSD Stokes V and I profiles. The reconstructed field is even more poloidal and axisymmetric, with a dipole component of $\simeq 650 \text{ G}$ only moderately tilted with respect to the rotation axis (by 10° to 25°). This magnetic topology is consistent with those of fully or largely convective main-sequence M dwarfs, whose convective zone is deeper than about half the stellar radius (Donati & Landstreet 2009), whereas the ratio of magnetic flux between small and large scales ($f_V/f_I = 0.22$) agrees with previous measurements (Morin et al. 2008b; Kochukhov 2021).

Whereas the Stokes I & V analysis gives a more reliable description of the overall strength and geometry of the average large-scale and small scale fields at the surface of AU Mic, the Stokes V analysis better accounts for the seasonal evolution of the large-scale field. The difference in large-scale field strength between these two approaches reflects that some of the large-scale magnetic topology of AU Mic (and in particular the axisymmetric component) may remain undetected through Stokes V data only, as a result of the almost perpendicular orientation of the stellar rotation axis with

respect to the line of sight (assuming that the orbital plane of the planets coincides with the equatorial plane of the star). Collecting Stokes Q and U (in addition to Stokes V) data of AU Mic would help in this respect, as these Zeeman signatures should be detectable in AU Mic and could be used to efficiently differentiate between both magnetic configurations (see Fig. C1 in supplementary material). An accurate estimate of the large-scale dipole field of AU Mic is also needed for studies of potential interactions between the host star and its close-in planets (Kavanagh et al. 2021; Klein et al. 2022), or for space weather simulations in the system (Carolan et al. 2020; Alvarado-Gómez et al. 2022; Mesquita et al. 2022).

From the temporal evolution of Stokes V profiles in 2020 and 2021, we retrieve the average amount of latitudinal differential rotation shearing the surface of AU Mic, and find that the rotation rate at the equator Ω_{eq} and the difference in rotation rate between the equator and pole $d\Omega$ are equal to 1.299 and 0.037 rad d^{-1} , corresponding to rotation periods at the equator and pole of 4.84 and 4.98 d , respectively, and to a latitudinal shear equal to about two thirds that at the surface of the Sun. This amount of DR is typical to that found on partly convective low-mass stars (e.g. Hébrard et al. 2016). As the values derived at each epoch ($\Omega_{\text{eq}} = 1.3006 \pm 0.0004$ and $d\Omega = 0.0445 \pm 0.0014 \text{ rad d}^{-1}$ in 2020 and $\Omega_{\text{eq}} = 1.2970 \pm 0.0002$ and $d\Omega = 0.0298 \pm 0.0013 \text{ rad d}^{-1}$ in 2021) differ by more than 3σ , we can conclude that differential rotation at the surface of AU Mic is likely varying with time. We, none the less, caution that the unusual amount of intrinsic variability observed for this star may have induced part of this discrepancy, making it essential to monitor the star over at least several months to minimize its impact and ensure we can derive reliable estimates of the DR parameters.

RVs inferred with the LBL technique (Artigau et al. 2022) from the SPIRou spectra of AU Mic processed with APERO (Cook et al. 2022) show an overall scatter of 31 m s^{-1} RMS over the full observing period, with some seasons (e.g. 2020) exhibiting a smaller than average dispersion (24 m s^{-1}). This is a factor of about 4 smaller than the average scatter at visible wavelengths (127 m s^{-1} RMS) reported by Zicher et al. (2022), illustrating how efficient SPIRou is to obtain precise RVs of active M dwarfs (e.g. Carmona et al. 2023). These RV variations are strongly modulated with a period of $4.866 \pm 0.004 \text{ d}$, marginally longer than that on which B_ℓ and $\langle B \rangle$ are modulated. We further obtain that RVs are well correlated, neither with B_ℓ nor with $\langle B \rangle$ but with the first time derivative of $\langle B \rangle$ ($R = 0.78$), similar to what was reported for Proxima (using the FWHM of the cross-correlation function as a proxy for $\langle B \rangle$; Suárez Mascareño et al. 2020). Using this correlation to filter RVs from the activity jitter improves the situation but leaves a significant fraction (about 45 per cent) of the jitter. A QP GPR fit to the RVs provides a more efficient filtering, leaving essentially no signal at the rotation period and its harmonics and aliases. The typical evolution time-scale of the activity jitter is found to be $136 \pm 21 \text{ d}$, larger than that of B_ℓ but consistent with that of $\langle B \rangle$. Although the dLW activity index provided by LBL does not correlate well with $\langle B \rangle$, we find that the strongest wPCA component $W_1(t)$ of all per-line dLW time series is strongly correlated with $\langle B \rangle$ in AU Mic ($R = 0.96$) and can thereby serve as a much better activity proxy than dLW itself (Cadieux et al. in preparation). Filtering RVs using the first time derivative of W_1 yields results similar to (though not better than) those achieved with $\langle B \rangle$. Machine Learning is apparently a promising alternative to GPR for filtering activity (Perger et al. 2023), with the advantage of being based on a physical background.

Modelling the RV signatures of transiting planets b and c (with the orbital periods and TESS transit times set to the values quoted in Szabó et al. 2022) at the same time as the activity jitter yields

semi-amplitudes of $K_b = 4.1_{-1.2}^{+1.8}$ and $K_c = 4.0_{-1.2}^{+1.7}$ m s^{-1} for planets b and c, with a residual RV scatter of 11.1 m s^{-1} RMS. This is consistent with previous results from optical data (where the activity jitter is $4\times$ larger, Zicher et al. 2022) for planet b, but smaller by a factor of 2 for planet c. We suspect that the difference mainly reflects residuals when filtering the strong activity jitter from optical data, that resulted in relatively large error bars on the semi-amplitudes of both planets (of 2.5 m s^{-1} , i.e. $1.5\text{--}2\times$ larger than ours). When looking at residuals in the periodogram of filtered RVs, we find excess power at a period of 33.4 d that hints at the presence of another planet in the system, dubbed candidate planet e. Fitting orbital parameters of planet e along with those of planets b and c and the hyper-parameters of the GP describing activity yields $K_e = 11.1_{-1.7}^{+2.1}$ m s^{-1} and $P_e = 33.39 \pm 0.10$ d, and slightly larger semi-amplitudes for planets b and c ($K_b = 4.5_{-1.2}^{+1.7}$ m s^{-1} , $K_c = 4.8_{-1.2}^{+1.6}$ m s^{-1}), with the RV signatures detected at a 6.5σ level for planet e and $\simeq 4\sigma$ level for b and c. We find that including candidate planet e gives a logarithmic Bayes factor of 16.3 for this model with respect to that featuring planets b and c only (plus activity), indicating that the detection is reliable, and induces a decrease in the residual RV scatter (now 10.4 m s^{-1} RMS). Fitting eccentricities of all 3 planets yields values compatible with zero (with error bars of 0.04, 0.07, and 0.09 for planets b, c, and e, respectively) along with a non-significant increase in marginal logarithmic likelihood, confirming that circular orbits for all 3 planets is the default model to be used here. We stress that the period of candidate planet e is close to a 1-yr alias of the Moon synodic period (32.1 d, see window function in Fig. 9) but distant from it by $13\times$ the error bar on the derived period, ensuring that both peaks are distinct. We none the less caution that this proximity is suspicious, hence why we choose to refer to planet e as a candidate planet at this stage. We also note that candidate planet e is close to a 4:1 resonance with planet b, and to a 7:1 resonance with the rotation of the star.

The derived semi-amplitudes yield masses of $10.2_{-2.7}^{+3.9}$, $14.2_{-3.5}^{+4.8}$, and $35.2_{-5.4}^{+6.7}$ M_\oplus for planets b, c, and e, respectively. The corresponding densities for planets b and c (whose radii are 3.55 ± 0.13 and $2.56 \pm 0.12 R_\oplus$, where R_\oplus notes the Earth radius Szabó et al. 2022) are $1.26_{-0.43}^{+0.68}$ and $4.7_{-1.6}^{+2.5}$ g cm^{-3} , i.e. about $3.7\times$ larger for c than for b whereas the opposite is usually observed in evolved multiplanet systems (but not for all, e.g. Leleu et al. 2021) as a result of the difference in equilibrium temperatures (593 ± 21 and 454 ± 16 K for b and c, respectively; Martioli et al. 2021, $\simeq 370$ K for candidate planet e using similar assumptions). However, the observed density contrast also reflects the fact that both planets did not yet complete their contraction process, in particular planet b that is still rather inflated (Zicher et al. 2022). Both planets are not expected to evolve in the same way as a result of cooling, contraction, or photoevaporation of the H/He atmosphere, given the difference in mass and distance from the star. In particular, given its higher equilibrium temperature possibly boosted by induction heating (Kislyakova et al. 2018), and its marginally lower mass, b is expected to increase its density more than c, hence reducing the density contrast between both. Predicting the evolution of b and c from their observed positions in a radius versus mass diagram (see Fig. 11) requires calculations with, e.g. the MESA models (Owen & Wu 2013), as in Zicher et al. (2022). The inflation of planet b makes it an ideal target for future atmospheric characterization, especially given its strong level of irradiation that should also extend its atmosphere and provide opportunities of investigating deeper atmospheric layers (García Muñoz et al. 2021). Whereas planet e alone should place the planetary system of AU Mic in the ‘ordered’ category recently defined by Mishra et al. (2023), planet d and e should put it in the ‘mixed’ class. In both cases,

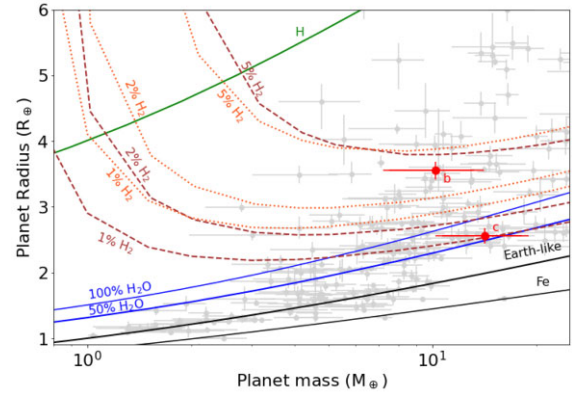


Figure 11. Mass–radius diagram for exoplanets whose mass and radius are known with a relative precision better than 30 percent (grey points). AU Mic b and c are shown with red filled circles and corresponding error bars, and are expected to contract with age (e.g. Owen & Wu 2013). Theoretical models of Zeng, Sasselov & Jacobsen (2016), Zeng et al. (2019) corresponding to various inner planet structures/compositions are depicted with black (100 percent iron and Earth-like), green (100 percent H) and blue (100 percent and 50 percent H_2O envelope) full lines. Models with a 1, 2, and 5 percent H_2 atmosphere with either an Earth-like (brown dashes) or a 50 percent water (orange dashes) interior are also shown.

AU Mic will bring valuable observational constraints on young planetary system architectures and their expected evolution with time.

Assuming it is located in the same orbital plane as transiting planets b and c and given the impact parameters of b and c (respectively equal to 0.17 ± 0.11 and $0.58 \pm 0.13 R_*$; Szabó et al. 2022), candidate planet e is probably not transiting or only through a grazing transit given the distance at which it orbits, i.e. 0.171 ± 0.005 au, as opposed to 0.0645 ± 0.0013 and 0.1101 ± 0.0022 au for planets b and c. No transit at this period has been reported yet, although the limited monitoring windows of TESS for AU Mic (28 d) would make it more difficult to detect (if it happens) than those of planets b and c. We note that the derived epoch of transit (or of conjunction) implies that if planet e is transiting, several transits should have been observed in TESS data (in sector #1 at BJD 2458449.3 \pm 2.9 and sector #27 at BJD 2459050.3 \pm 1.1) and potentially during CHEOPS #2 and #3 visits as well (at BJDs 2459083.7 \pm 1.0 and 2459117.1 \pm 0.9; Szabó et al. 2021). Since these data show no evidence of a transit, we conclude that candidate planet e is unlikely to transit.

By studying the stability of the b + c + e system, we find that candidate planet e can be stable on a Gyr time-scale for the orbital periods and modest eccentricities allowed by the RV data (see Fig. 12). The best-fitting orbital solution (see Table 4) is not in exact resonance with any of the other planets, implying that planet e is not able to significantly perturb the orbits of planets b and c nor to generate the TTVs of up to ± 10 min reported for planet b (Szabó et al. 2022). By scanning a range of values about those derived in our study for the parameters of planet e (mass, period, eccentricity, and argument of periastron) to investigate whether a reasonable fit to the observed TESS, Spitzer, and CHEOPS transit epochs was achievable, we obtain that no combination is able to reproduce transit data, even for orbital periods corresponding to a 4:1 resonance with planet b.

We also investigated whether candidate planet d, suggested to be orbiting between b and c and potentially causing the reported TTVs (Wittrock et al. 2023), is detectable in our data. We find no clear evidence of its presence and derive a 3σ upper limit on the amplitude of its RV signature ($K_d < 4.4 \text{ m s}^{-1}$) and on its minimum mass

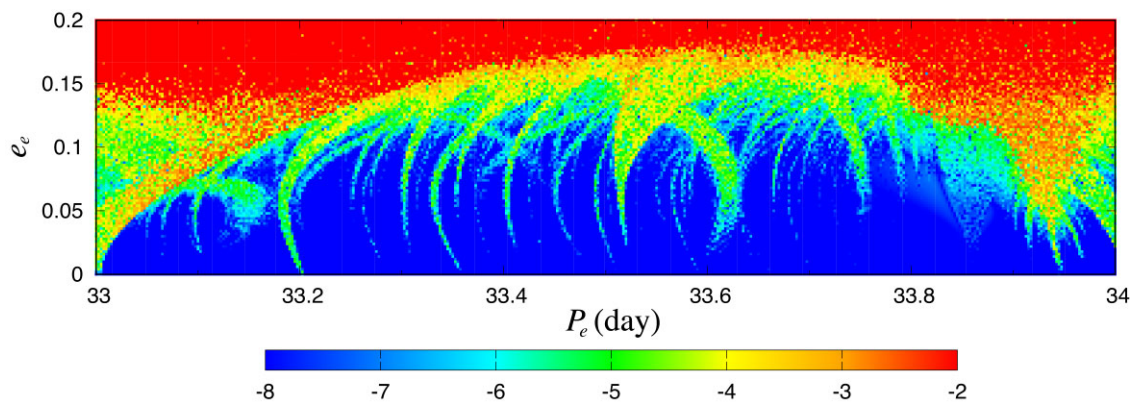


Figure 12. Period versus eccentricity stability diagram for candidate planet e of the b + c + e AU Mic system. The phase space of the system is explored by varying the period (in d) and eccentricity of candidate planet e about the value derived in this work (Table 4). For each initial condition, the system is integrated over 5 kyr with the symplectic integrator SABAC4 (Laskar & Robutel 2001). A stability criterion is derived from the frequency analysis of the mean longitude (Laskar 1993). The chaotic behaviour is quantified by the variation in the mean motion, with the colour scale coding the decimal logarithm of the mean motion variation (Correia et al. 2010). The red areas corresponds to unstable orbits, and the blue ones to orbits that are presumably stable on a Gyr time-scale.

($M_d < 11.4 M_{\oplus}$), consistent with the prediction ($\simeq 1 M_{\oplus}$; Wittrock et al. 2023). Besides, we confirm that b + c + d is stable for the 12.74-d period and low-eccentricity orbit of planet d suggested by Wittrock et al. (2023), whereas b + c + d + e, though less stable, should still be able to survive on long time-scales (see Fig. E1 in supplementary material). We also verified that the simulated TTVs are much more consistent with the transit timings of planets b and c once candidate planet d is included (see Fig. E2 in supplementary material, in agreement with Wittrock et al. 2023).

Finally, we studied the Pa β and He I lines and in particular the temporal modulation of their equivalent widths (EWVs) over our 4 observing seasons. We find that these lines exhibit clear modulation with periods that are consistent with the rotation period of the star, despite showing both a significant level of intrinsic variability. EWVs are clearer for Pa β (than for He I) and are found to correlate reasonably well, for this line, with our estimates of the small-scale field $\langle B \rangle$. Both Pa β EWVs and $\langle B \rangle$ slowly decrease with time over the 3 yr of our observing campaign, suggesting that AU Mic may be progressing towards activity minimum along its putative cycle (Ibañez Bustos et al. 2019). As opposed to Klein et al. (2022), we find no clear evidence that either line is modulated at the period of the system planets. The low-significance peaks (FAP of $\simeq 10$ per cent) observed close to the orbital periods of planets b and c in the periodogram of He I EWVs are similar in strength to many others and cannot reliably be considered as a sign of, e.g. star-planet interaction between AU Mic and its inner planets.

We will pursue our spectropolarimetric monitoring of AU Mic with SPIRou for another 2 yr within the context of the new SPICE Large Programme, that was allocated 175 nights of CFHT time from late 2022 to mid 2024, and whose aim is to consolidate and enhance the results of the SLS. The first goal is to firmly ascertain the existence of candidate planets e and possibly d, and improve at the same time the precision on the mass estimates of all planets, a rather tricky task given the extreme activity level of AU Mic, even in the nIR where the RV activity jitter is $4\times$ smaller than at visible wavelengths. With its system of young planets (2 of which transiting) that are still likely evolving with time, AU Mic is an ideal laboratory to test and constrain models of planet formation and evolution, and to investigate the atmospheric composition of young inflated planets. Besides, we also aim at pursuing the magnetic monitoring of AU Mic on a longer time-scale to investigate whether the poloidal and toroidal components of

large-scale field vary in a cyclic way (e.g. Ibañez Bustos et al. 2019), switching sign as they do on the Sun, and to document the changes in the small-scale field as the large-scale field evolves with time. Given that no clear sign switch was observed yet in either field component, the present data suggest that, if there is a cycle, the period is at least 5 years. We stress that having access to Stokes Q and U observations of AU Mic with SPIRou for at least a partial season, and thereby complement the Stokes V and I data to be collected with SPICE, would further enhance our ability to consistently model the magnetic topology and verify the assumptions on which the results presented in this paper rely. More generally, multiwavelength multiinstrument monitoring campaigns of AU Mic, involving in particular precision photometry from space (TESS, CHEOPS and later-on PLATO), optical and nIR high-resolution spectropolarimetry and velocimetry (e.g. ESPaDOnS, SPIRou, CRIRES + for longer wavelengths), and low-resolution nIR spectroscopy from space with the JWST, especially during transits, would be a must to characterize in detail this young multiplanet system of our immediate neighbourhood.

ACKNOWLEDGEMENTS

This project received funds from the European Research Council (ERC) under the H2020 research & innovation program (grant agreements #740651 NewWorlds, #742095 SPIDI, #865624 GPRV, #716155 SACCRED, #817540 ASTROFLOW), the Agence Nationale pour la Recherche (ANR, project ANR-18-CE31-0019 SPlaSH) and the Investissements d’Avenir program (project ANR-15-IDEX-02). SHPA and EM acknowledge funding from FAPEMIG, CNPq, and CAPES, while ACMC acknowledges project funds UIDB/04564/2020, UIDP/04564/2020, and PTDC/FIS-AST/7002/2020. We thank F. Ménard and an anonymous referee for valuable comments on an earlier version of the manuscript.

Our study is based on data obtained at the CFHT, operated by the CNRC (Canada), INSU/CNRS (France) and the University of Hawaii. The authors wish to recognize and acknowledge the very significant cultural role and reverence that the summit of Maunakea has always had within the indigenous Hawaiian community. We are most fortunate to have the opportunity to conduct observations from this mountain. This work also benefited from the SIMBAD CDS data base at URL <http://simbad.u-strasbg.fr/simbad> and the ADS system at URL <https://ui.adsabs.harvard.edu>.

DATA AVAILABILITY

Most data underlying this paper are part of the SLS, and will be publicly available from the Canadian Astronomy Data Center by 2024, February while the PI and DDT data are already public.

REFERENCES

- Afram N., Berdyugina S. V., 2019, *A&A*, 629, A83
 Alvarado-Gómez J. D. et al., 2022, *ApJ*, 928, 147
 Artigau É. et al., 2022, *AJ*, 164, 84
 Baraffe I., Homeier D., Allard F., Chabrier G., 2015, *A&A*, 577, A42
 Blinova A. A., Romanova M. M., Lovelace R. V. E., 2016, *MNRAS*, 459, 2354
 Boccaletti A. et al., 2015, *Nature*, 526, 230
 Boccaletti A. et al., 2018, *A&A*, 614, A52
 Cale B. L. et al., 2021, *AJ*, 162, 295
 Carmona A. et al., 2023, preprint (arXiv:2303.16712)
 Carolan S., Vidotto A. A., Plavchan P., Villarreal D'Angelo C., Hazra G., 2020, *MNRAS*, 498, L53
 Chabrier G., Gallardo J., Baraffe I., 2007, *A&A*, 472, L17
 Chib S., Jeliakov I., 2001, *J. Am. Stat. Assoc.*, 96, 270
 Cifuentes C. et al., 2020, *A&A*, 642, A115
 Cook N. J. et al., 2022, *PASP*, 134, 114509
 Correia A. C. M. et al., 2010, *A&A*, 511, A21
 Cristofari P. I. et al., 2022a, *MNRAS*, 511, 1893
 Cristofari P. I. et al., 2022b, *MNRAS*, 516, 3802
 Cristofari P. I. et al., 2023, *MNRAS*, 522, 1342
 Cutri R. M. et al., 2003, VizieR Online Data Catalog, p. II/246
 David T. J., Petigura E. A., Luger R., Foreman-Mackey D., Livingston J. H., Mamajek E. E., Hillenbrand L. A., 2019, *ApJ*, 885, L12
 Delchambre L., 2015, *MNRAS*, 446, 3545
 Donati J., Landstreet J. D., 2009, *ARA&A*, 47, 333
 Donati J.-F., Semel M., Carter B. D., Rees D. E., Collier Cameron A., 1997, *MNRAS*, 291, 658
 Donati J.-F., Collier Cameron A., Petit P., 2003, *MNRAS*, 345, 1187
 Donati J.-F. et al., 2006, *MNRAS*, 370, 629
 Donati J. F. et al., 2020, *MNRAS*, 498, 5684
 Dotter A., Chaboyer B., Jevremović D., Kostov V., Baron E., Ferguson J. W., 2008, *ApJS*, 178, 89
 Feiden G. A., 2016, *A&A*, 593, A99
 Finocietty B., Donati J. F., 2022, *MNRAS*, 516, 5887
 Finocietty B. et al., 2021, *MNRAS*, 508, 3427
 Finocietty B. et al., 2023, *MNRAS*, 520, 3049
 Gaia Collaboration, 2021, *A&A*, 649, A1
 Gaidos E. et al., 2014, *MNRAS*, 443, 2561
 Gallenne A., Desgrange C., Milli J., Sanchez-Bermudez J., Chauvin G., Kraus S., Girard J. H., Boccaletti A., 2022, *A&A*, 665, A41
 García Muñoz A., Fossati L., Youngblood A., Nettelmann N., Gandolfi D., Cabrera J., Rauer H., 2021, *ApJ*, 907, L36
 Haywood R. D. et al., 2014, *MNRAS*, 443, 2517
 Haywood R. D. et al., 2022, *ApJ*, 935, 6
 Hébrard É. M., Donati J. F., Delfosse X., Morin J., Moutou C., Boisse I., 2016, *MNRAS*, 461, 1465
 Hirano T. et al., 2020, *ApJ*, 899, L13
 Ibañez Bustos R. V., Buccino A. P., Flores M., Martínez C. I., Maizel D., Messina S., Mauas P. J. D., 2019, *MNRAS*, 483, 1159
 Kalas P., Liu M. C., Matthews B. C., 2004, *Sci.*, 303, 1990
 Kavanagh R. D., Vidotto A. A., Klein B., Jardine M. M., Donati J.-F., Ó Fionnagáin D., 2021, *MNRAS*, 504, 1511
 Kiraga M., 2012, *AcA*, 62, 67
 Kislyakova K. G., Fossati L., Johnstone C. P., Noack L., Lüftinger T., Zaitsev V. V., Lammer H., 2018, *ApJ*, 858, 105
 Klein B. et al., 2021, *MNRAS*, 502, 188
 Klein B. et al., 2022, *MNRAS*, 512, 5067
 Kochukhov O., 2021, *A&A Rev.*, 29, 1
 Kochukhov O., Reiners A., 2020, *ApJ*, 902, 43
 Landi degl'Innocenti E., Landolfi M., 2004, Polarisation in spectral lines. Kluwer Academic Publishers, Dordrecht/Boston/London
 Laskar J., 1993, *Phys. D Nonlinear Phenom.*, 67, 257
 Laskar J., Robutel P., 2001, *Celest. Mech. Dyn. Astron.*, 80, 39
 Lehmann L. T., Donati J. F., 2022, *MNRAS*, 514, 2333
 Leleu A. et al., 2021, *A&A*, 649, A26
 López-Valdivia R. et al., 2021, *ApJ*, 921, 53
 Maldonado J. et al., 2020, *A&A*, 644, A68
 Malo L., Doyon R., Feiden G. A., Albert L., Lafrenière D., Artigau É., Gagné J., Riedel A., 2014, *ApJ*, 792, 37
 Mamajek E. E., Bell C. P. M., 2014, *MNRAS*, 445, 2169
 Martioli E. et al., 2020, *A&A*, 641, L1
 Martioli E., Hébrard G., Correia A. C. M., Laskar J., Lecavelier des Etangs A., 2021, *A&A*, 649, A177
 Mesquita A. L., Rodgers-Lee D., Vidotto A. A., Kavanagh R. D., 2022, *MNRAS*, 515, 1218
 Miret-Roig N. et al., 2020, *A&A*, 642, A179
 Mishra L., Alibert Y., Udry S., Mordasini C., 2023, *A&A*, 670, A68
 Morales J. C., Gallardo J., Ribas I., Jordi C., Baraffe I., Chabrier G., 2010, *ApJ*, 718, 502
 Morin J. et al., 2008a, *MNRAS*, 384, 77
 Morin J. et al., 2008b, *MNRAS*, 390, 567
 Morin J., Donati J., Petit P., Delfosse X., Forveille T., Jardine M. M., 2010, *MNRAS*, 407, 2269
 Morrell S., Naylor T., 2019, *MNRAS*, 489, 2615
 Owen J. E., Wu Y., 2013, *ApJ*, 775, 105
 Pécaut M. J., Mamajek E. E., 2013, *ApJS*, 208, 9
 Perger M. et al., 2023, *A&A*, 672, A118
 Plavchan P. et al., 2020, *Nature*, 582, 497
 Reiners A. et al., 2022, *A&A*, 662, A41
 Ryabchikova T., Piskunov N., Kurucz R. L., Stempels H. C., Heiter U., Pakhomov Y., Barklem P. S., 2015, *Phys. Scr.*, 90, 054005
 Siess L., Dufour E., Forestini M., 2000, *A&A*, 358, 593
 Skilling J., Bryan R. K., 1984, *MNRAS*, 211, 111
 Strugarek A., Brun A. S., Matt S. P., Réville V., 2015, *ApJ*, 815, 111
 Suárez Mascareño A. et al., 2020, *A&A*, 639, A77
 Suárez Mascareño A. et al., 2021, *Nat. Astron.*, 6, 232
 Szabó G. M. et al., 2021, *A&A*, 654, A159
 Szabó G. M. et al., 2022, *A&A*, 659, L7
 Van Eylen V. et al., 2019, *AJ*, 157, 61
 Wittrock J. M. et al., 2023, preprint (arXiv:2302.04922)
 Zanni C., Ferreira J., 2013, *A&A*, 550, A99
 Zeng L., Sasselov D. D., Jacobsen S. B., 2016, *ApJ*, 819, 127
 Zeng L. et al., 2019, *Proc. Natl. Acad. Sci.*, 116, 9723
 Zicher N. et al., 2022, *MNRAS*, 512, 3060

SUPPORTING INFORMATION

Supplementary data are available at *MNRAS* online.

Table A1 Observation log. All exposures consist of 4 sub-exposures of equal length, except that marked with an ‘x’ for which only 2 of the 4 sub-exposures could be used.

Figure B1 Observed (thick black line) and modelled (thin red line) LSD Stokes *V* profiles of the photospheric lines of AU Mic, for seasons 2019 September–November (top left), 2020 April–November (bottom left), 2021 June–November (top right) and 2022 May–June (bottom right).

Figure C1 Calculated LSD Stokes *Q* (top panel) and *U* (bottom panel) signatures associated with the reconstructed magnetic topologies of AU Mic for season 2020 April–November, derived with the Stokes *V* (black line) and Stokes *I* & *V* (red line) analyses outlined in Sections 5.2 and 5.3 and shown in Figs 4 (second top row) and 5.

Figure D1 Spectra of AU Mic in the region of the He I triplet (top panel) and Pa β line (bottom panel), in the stellar rest frame.

Figure E1 Same as Fig. 12 for candidate planet d in the case of the b + c + d (top panel) and b + c + d + e (bottom panel) systems.

Figure E2 Predicted TTVs for transiting planets b (top) and c (bottom), in the b + c + e (red line) and b + c + d + e (green line), with the mass of candidate planet d set to $0.68 M_{\oplus}$ cases, compared with the transit timings derived by TESS, Spitzer and CHEOPS (Szabó et al. 2022, black open circles,).

Please note: Oxford University Press is not responsible for the content or functionality of any supporting materials supplied by the authors. Any queries (other than missing material) should be directed to the corresponding author for the article.

This paper has been typeset from a $\text{\TeX}/\text{\LaTeX}$ file prepared by the author.